Bachelor of Science

Visualization and Analysis of Vortex Propagation from a Jet Pump

Author:
Koen 't Hart

Supervisor:
Ir. J.P. Oosterhuis

Chairperson:
Prof. Dr. Ir. T.H. van der Meer

External Examiner:
dr. H.K. Hemmes

A thesis submitted in fulfilment of the requirements for the degree of Bachelor of Science

at the

Research Group of Thermal Engineering

in the

Department of Engineering Technology

September 2014

UNIVERSITEIT TWENTE.

UNIVERSITY OF TWENTE

Abstract

Faculty CTW
Department of Engineering Technology

Bachelor of Science

Visualization and Analysis of Vortex Propagation from a Jet Pump

by Koen 'T HART

Traveling wave thermoacoustic engines lose efficiency due to Gedeon streaming. If a jet pump is applied to the engine it counteracts the streaming by suppressing the time-averaged mass flux through the closed loop of the engine. Placing the jet pump inside the engine creates certain flow field effects due to “minor losses”.These flow field effects are oscillatory and have not been qualitatively recorded. The set-up used at the University of Twente to create acoustic sound waves allows flow visualization of the flow field generated by the jet pump. A high speed camera records smoke inserted with a smoke wire.

Vortices are found in the recorded images, and the purpose of this research is to create an algorithm to trace these vortices as they propagate through the flow field. The algorithm also calculates the speed with which they propagate but this is not the main focus. The created algorithm is analyzed using ROC-curves to determine if the algorithm is beneficial for the detection of vortices. The algorithm needs the input of some variables to allow proper detection, the influence of these variables is documented. There is a relation between the frequency of the acoustic sound wave and the size, speed and propagating distance of vortices. The variables therefore need adjusting for the vortices of higher acoustic sound waves. The development of the algorithm showed the potential of using these algorithms in the analysis of the other flow field effects. Further improvements are needed to make the algorithm more robust for reliable data collection

Acknowledgements

To start I would like to thank Joris Oosterhuis for the supervision during this bachelors assignment. Thanks to his quick acceptance I was able to do this assignment on such short notice. His help, guidance and great feedback contributed to the quality of this bachelors assignment. Furthermore the approach of Theo van der Meer with the weekly monday morning meeting created a platform for open discussion, encouragement and creativity. These meetings would be pointless though without the contribution of the participating members: Simon, Citra and Rob. I want to thank Citra personally too, for allowing me to help with her master thesisn, through which I quickly got familiar in the set-up and the theory of thermoacoustics. Joost also deserves some recognition for putting me in touch with Joris.

Thanks also go out to my friends(especially Mateo for lunching and working hard with me every day, and Jorrit for providing dinner), my girlfriend Bella, parents Edith and Erik, sister Robin and the rest of my family for their unending support and always present love.

Contents

Chapter 1

Introduction

This research aims to study the flow field near a jet pump in a thermoacoustic setup. The study focuses on registering vortices propagating from the jet pump, in images recorded with a high speed camera, with Matlab software. The expected results consist of an algorithm which tracks the propagating vortices for a wide range of images with the required accuracy.

This thesis will give a basic explanation of thermoacoustics, to understand the streaming effects and thus the reason for researching the jet pump. Furthermore the process and the experimental setup for image acquisition is described. The final step of the thesis is showing the post-processing steps and tools considered and applied, ending with the conclusion on the accuracy of the developed algorithm and possibilities for future improvements.

1.1 Thermoacoustic Devices

Thermoacoustics, as the name suggests, consists of two physical phenomena:

- Acoustics is the science of all mechanical waves (i.e. vibration, sound, ultrasound and infrasound) in a particular medium (i.e. gasses, solids and liquids).
- Thermodynamics is the transfer of energy from location with a high temperature to location with a low temperature.

This interaction is called thermoacoustics, wherein a generated temperature difference is used to create sound waves and vice versa. A device using thermoacoustic principles is called a thermoacoustic device. These devices use acoustic waves, in a channel where a temperature gradient is present, to cause thermal expansion and contraction.

If these are traveling waves, the thermoacoustic device is theoretically able to achieve a Stirling efficiency[2]. An example of such a device is the Los Alamos National Laboratory (LANL) thermoacoustic traveling wave engine shown in Figure 1.1. This particular engine has been a reference for many studies including this thesis.

1.1.1 A Brief History

To get a better understanding of thermoacoustic devices it is necessary to have a background in its history. Thermoacoustic effects have been noticed many years ago. For instance, glassblowers experienced sound generation by heating a closed-end tube. This became known as the Sondhauss effect in 1850[9]. Air is heated at the closed end, and this consequentially increases the pressure. The air then flows to the cool open end, transferring heat to the wall of the tube until it briefly compresses a small part of the atmosphere. This creates a propagating sound wave. Shortly after this compression, the atmosphere pushes air back into the tube to repeat the cycle. The Dutch professor P.L. Rijke invented a similar tube in 1859 but this particular variant requires a steady flow of air with two open ends[8].

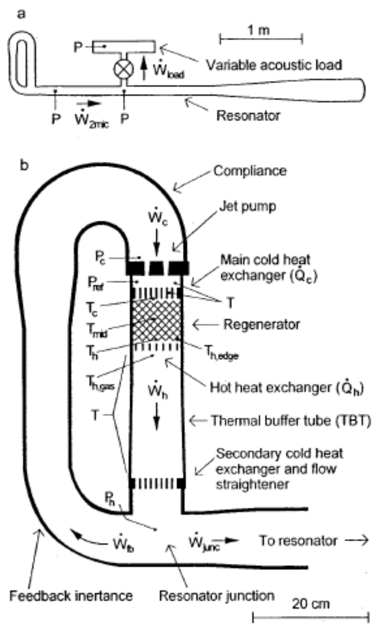

FIGURE 1.1: the Los Alamos National Laboraty researched engine[2].

In 1877 it was John William Strutt, known as the 3^{rd} Baron of Rayleigh, who wrote a book on sound waves and researched the Rijke and Sondhauss tubes. Lord Rayleigh wrote down the qualitative explanations for the effects and defined a criterion for thermoacoustic effects as:

> Lord Rayleigh - *"If heat be given to the air at the moment of greatest condensation or taken from it at the moment of greatest rarefaction, the vibration is encouraged"*[28]

This is a criterion for a heat-driven oscillation. Rayleigh basically states that if heat is given or removed at either the highest or lowest density, oscillations are more likely to happen. He described a relation between heat-injection and density variation.

After Lord Rayleigh's discovery, research continued on the Sondhauss tube, the Rijke tube[3] and the Taconis oscillations[14] which are similar to the Sondhauss tube but with cryogenic temperatures. Scientists like Lord Rayleigh, Kirchoff and Kramers created a formal theoretical study of thermoacoustics but it was not until 1969 with Rott's breakthrough in modeling thermoacoustic phenomena that major progress was made[30].

N. Rott described acoustic oscillations for gas in a channel with an axial temperature gradient, where its dimensions were out of proportion with the sound wavelength. The lateral channel dimensions were in the order of the gas thermal penetration depth δ_k. Penetration depth is the thickness of the layer of gas where heat can diffuse in oscillations, typically in the order of 1mm. That is much shorter than the acoustic wavelength, which is typically 1m for thermoacoustic cases. Rott's linear theory has been verified and found quantitatively accurate on multiple tests[43].

After this, thermoacoustics has become an important chapter in heat pumps (transfer of heat by applying work) and prime movers (generation of work by applying heat gradient). A similar research has been done by G.W. Swift and many others, but it was Swift who implemented Rott's theory to create thermoacoustic devices[31]. It was Backhaus with the contribution of Swift who invented the thermoacoustic engine in Figure 1.1 in 1999. This engine has been constructed by limiting the number of moving parts as motivation, a topic where many researchers are working on[27][35][5][6][42]. The engine's main part is the regenerator, with a hot and a cold heat exchanger, which creates the temperature gradient needed for the conversion of heat to acoustic power. The lack of moving parts proved to be a challenge, it introduced many side affects which lowered the efficiency drastically[2]. One of these side effects is acoustic streaming, a mean mass flux through the torus of the engine.

1.1.2 Acoustic Streaming

Rayleigh started researching acoustic streaming more then a century ago. However, some effects are still not entirely understood. Acoustic streaming is a net mean flow across the acoustic system. This flow is the result of the generated sound waves, but it is not a linear effect. This makes analysis with linear acoustic theory impossible. There is more than one type of acoustic streaming with different characteristics but the common effect is efficiency loss. In a looped geometry like the Backhaus and Swift engine, Gedeon streaming can occur. This can be prevented when a jet pump is added.

1.1.2.1 Gedeon Streaming

This type of streaming is based on a net mean mass flow typical for traveling wave devices. It depends on the dissipation mechanism in the flow field and the phase between acoustic velocity and density. Gedeon streaming is relevant for oscillatory thermoacoustic engines, and an example of the effect can be seen in Figure 1.2. Gedeon assumed the pressure drop, ΔP, linear with velocity U. With that assumption, Gedeon proved that to have mean mass flow, it is necessary for the flow to fulfill a condition. The flow needs a resistance in its path which can be seen as an asymmetrical return path to build up pressure. These conditions can be fulfilled through device geometry, density, pressure and/or temperature variation[4].

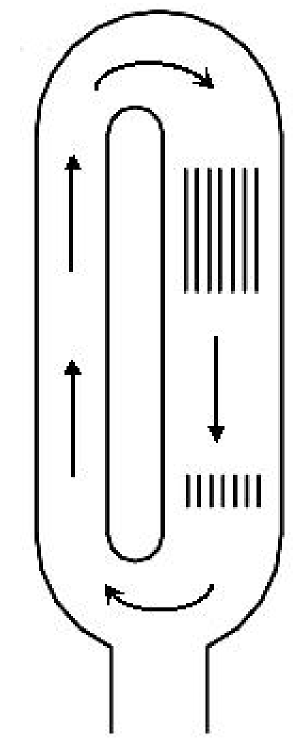

FIGURE 1.2: An example of Gedeon streaming in a torus[31].

It is essential for the performance of a thermoacoustic engine to achieve complete elimination of Gedeon streaming. Gedeon streaming leads to a time-averaged mass flux $\dot{M}_2$ inside the torus shape of the thermoacoustic engine[4]. This torus allows the mass flux to return via an asymmetrical path. Equation 1.1 is for time-averaged mass flux.

$$\dot{M}_2 = \frac{Re[\rho_1 \tilde{U}_1]}{2} + \rho_m U_{2,0} \tag{1.1}$$

Where $U_{2,0}$ is the second order time-independent volumetric velocity[2]. The time-averaged acoustic power flow is written as $\frac{Re[\rho_1 \tilde{U}_1]}{2} = \dot{W}$. In a case where there are no actions taken to impose a $U_{2,0}$ which cancels the first term, the time-averaged mass flux would transfer heat from the hot to the cold heat exchanger. This causes undesirable heat leak and efficiency loss.

Backhaus and Swift state that a non-zero $U_{2,0}$ must flow around the torus to enforce $\dot{M}_2 = 0$. Flow is generated through pressure difference. Hence we would need an extra part called the jet pump to apply the required pressure difference to cancel out the mass flux[32].

1.1.3 Jet Pump

A jet pump is a cylindrical part consistent of two openings and a tapered section connecting them. As can be seen in Figure 1.3, the jet pump has asymmetric radii R_b and $R_{s,eff}$ where the flow is allowed to enter. The jet pump constricts flow and forces it through its two openings of different sizes. This causes a sudden contraction and expansion of the flow. Contraction occurs when the flow comes from the outer tube to either the big or small opening in the jet pump. Expansion occurs when the flow is reversed and the opposite happens. This means due the oscillatory motion of the flow, both expansion and contraction occur.

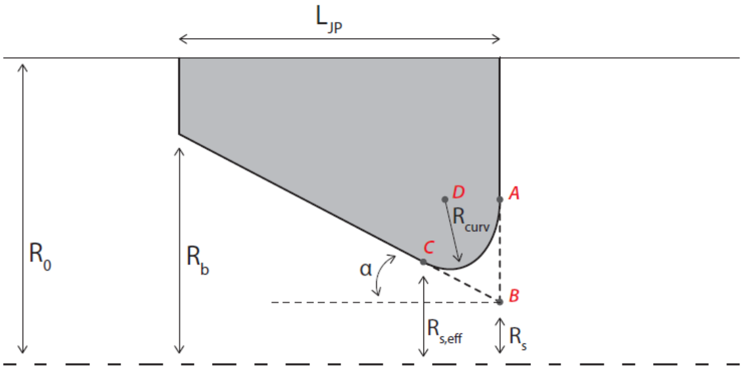

FIGURE 1.3: A sliced jet pump where the dotted line represents a symmetrical axis. The dimensions are required to define the geometry of the jet pump[7].

If the cross-sectional area of a pipe gradually decreases, mass conservation requires an increase in mean velocity and a decrease in pressure according to Bernoulli. The jet pump makes this transition abruptly which gives rise to flow separation, vortex shedding, turbulence, and jetting[26]. These dissipative effects are hydrodynamic and cause the Bernoulli equation to be invalid. More so, the abrupt transition generates an extra pressure drop known as "minor losses". This pressure drop allows us to generate a $U_{2,0}$ to control the mean mass flux $\dot{M}_2$ from Equation 1.1.

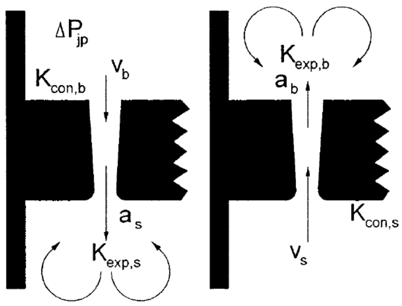

FIGURE 1.4: Schematic diagram of a jet pump. With flow going from a large cross-sectional a_b to the small cross-sectional a_s on the left and in reverse on the right.

Figure 1.4 shows two different states of flow. Flow is either going from the large cross-sectional a_b to the small cross-sectional a_s or in reverse. This results in a ΔP_{jp} which is dependent on the density of the fluid ρ, velocity of the flow U^2 and a minor loss coefficient K. This minor loss coefficient is not symmetric so there is a $K_{exp\,s,b}$ and $K_{con\,s,b}$ for contracting and expanding the flow, the s and b are respectively the small and large cross-sectional area. Petculescu states that although these coefficients are only valid in steady flow, they also fulfill the “Iguchi Hypothesis”[26]. Iguchi and Ohmi performed extensive measurements showing the results of an orifice placed across the bottom of a tube. These results can be described as quasi-steady, so we can separate the directions of flow[16]. That means that the flow in Figure 1.4 can be calculated separately and added later to find a net pressure drop across the system.

This is one of the assumptions made to calculate ΔP_{jp} defined by the dimensions of the jet pump. Two other assumption are: stating that we are able to add the “minor loss” coefficients for both directions of flow and that the velocity in the jet pump $U_{1,jp}$ is harmonic. Backhaus and Swift made these assumptions to derive Equation 1.2, this equation is used for the design of jet pumps[2].

$$\Delta \bar{p_{jp}} = \frac{\rho_0 \left|U_{1,jp}\right|^2}{8a_s} \left[(K_{exp\,s} - K_{con\,s}) + \left(\frac{a_s}{a_b}\right)^2 (K_{exp\,b} - K_{con\,b}) \right] \tag{1.2}$$

ρ_0 is the mean density of the fluid flowing through the jet pump. Equation 1.2 is used to specify the parameters of the jet pump geometry. With this geometry and computational fluid dynamics software, the jet pump designs are simulated. To validate these simulations and research suggesting that the assumption of the ”Iguchi hypothesis” does not hold up for higher taper angles, we want to visualize the flow field near the jet pump[34]. If the flow field is made visible, the dissipative effects described above should be detected and those effects can be quantitatively analyzed.

1.2 Flow Visualization

Flow visualization is a means to making a flow field visible and allows an analysis of the flow effects. These effects happen in fluids which are typically translucent, and therefore the effects remain invisible. If we want to record the images which merit flow visualization, we need to add an observable foreign material. The motion this observable material undergoes is representative for the flow effects taking place in the region of interest(ROI). Meaningful images can also be created with an optical method. If density changes in the flow field are sufficiently large, light rays will be disturbed when passing through. This optical disturbance can be recorded using Schlieren photography and is representative for the flow field. Figure 1.5 and 1.6 are examples of options for both methods. Previous research done in flow visualization methods concluded that the addition of foreign particles is most suitable for this situation. This is because the density changes caused by acoustic waves are too small for any optical method to detect[21].

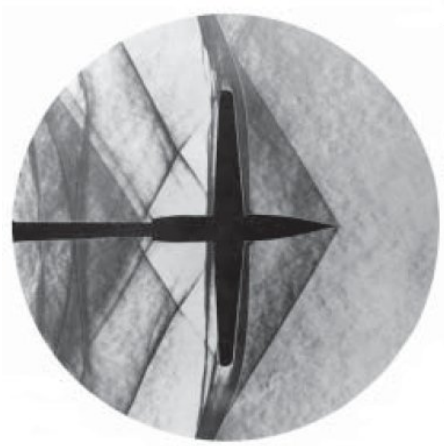

FIGURE 1.5: Schlierenfoto Mach 1-2 gerader Flügel[39].

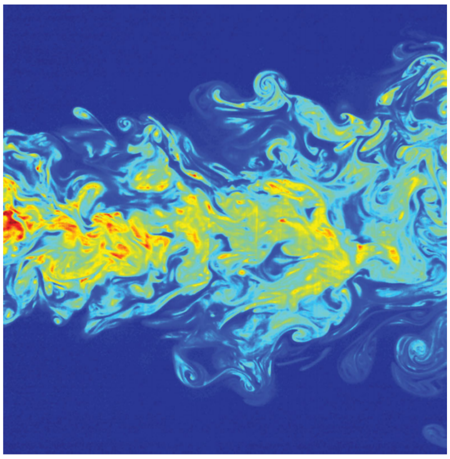

FIGURE 1.6: The instantaneous concentration field in the far field of a turbulent jet. Made with a laser and foreign fluid reactive to light[36].

1.2.1 Foreign Materials

The common element for this type of visualizations is the addition of a foreign material. The chosen material should not disturb the flow. For the same reason, insertion is a delicate process. The medium flowing through the jet pump is air, thus transparent and gaseous, that allows for the addition of either smoke or particles.

1.2.1.1 Smoke

Smoke is widely used as a tracer for visualization. Smoke can be used either as a smoke screen or as smoke lines[21]. Smoke's natural buoyancy is useful because it allows the smoke to move as one homogeneous tracer only to be disturbed by the flow. There exists a great variety of smoke types, not limited to combustion products but any gas that is visible without optical techniques. The optimal smoke would be nontoxic, naturally buoyant, stable against mixing and well visible[22].

These requirements prove hard for smoke to fulfill. Inherently all smoke is toxic to a certain degree. Smoke also has the tendency to accumulate and fill the ROI with smoke or any deposit it might generate. Flow visualization with smoke is a consideration between visibility; its susceptibility to disturbance, accumulation and the injection method.

1.2.1.2 Particles

Another option is to add numerous tracer particles to the air flow, these particles are in the order of 10 to 100 micrometers. The particles size is an assessment between the response time to the air flow and the quantity of scattered light. The concentration of injected particles depends on the used technique. Laser Doppler velocimetry uses a lower concentration, such a concentration that individual particle tracking is possible between images. This allows the technique to measure particle speed at specified points inside the ROI[21]. Another technique, particle image velocimetry (PIV), uses a higher concentration so that particle tracking between images is not certain anymore. This technique uses a laser, a camera and a synchronizer. By illuminating the particles with a laser sheet a 2D representation of the velocity is made. The particles are illuminated for a short time, just for two laser pulses. This results in two images which can be cross correlated to calculate vorticity and velocity. If the images are recorded in stereoscopy which involves two cameras, PIV can also record a 3D representation of the flow field.

Drawbacks of PIV are the particles involved. The particle's density will inhibit them from following the flow field's motion. The density has to match up with the fluid, otherwise the natural buoyancy is not present. If the density of the particles cannot be changed, there is the option to change the density of the fluid. Changing the fluid results in a change in Reynolds number. Changing the Reynolds number for an experiment comes with a change in fluid velocity or the object of interest's size. Also with the use of multiple cameras, lasers and the particles there are cost and safety concerns.

Therefore the choice is made to visualize the flow with smoke. This method is cheap and easily reproducible with a constant performance. The drawbacks of smoke are solved by adjusting the duration of injection or by geometric changes to the set-up. This proves to be more cost friendly than rebuilding the experimental set-up to allow laser use.

Chapter 2

Method

2.1 Experimental Set-up

In this section, the experimental set-up is briefly explained. [1].

Originally constructed at the TU Eindhoven[1], the set-up is re-purposed by the Thermal Engineering research group at University of Twente to perform measurements in thermoacoustics. The set-up consists of three main parts: a loudspeaker, a cone and the resonator section showed in figure 2.1. The loudspeaker creates an acoustic wave which is amplified by the contraction of the diameter from cone to resonator. The resonator can be modified to fit different purposes. For flow field visualization a test section is placed. The jet pump, as well as the smoke injection system, can be mounted inside this test section[34][7]. The test section is a clear acrylic (PMMA) glass tube to allow flow visualization recording. The PMMA material is cheaper to manufacture and is a

[1]The full explanation of specifics about the set-up can be found in the thesis of D. van der Gun[12]

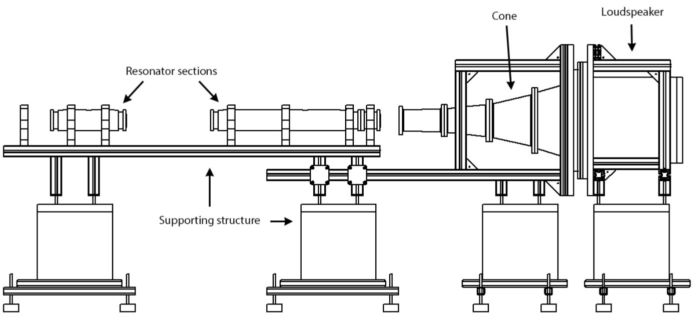

FIGURE 2.1: A schematic drawing of the experimental set-up used throughout the experiments[21].

lot less fragile than glass. However, the downside of using a cylindrical shape are the reflections of the light. The jet pump test section is showed in Figure 2.2.

The ending of the resonator tube, also called the termination, can be varied. The termination is: closed, opened or configured with a resonator. This resonator simulates a traveling wave going through the test section and works for a pre-determined frequency[34]. The visualizations for this thesis are done with the open configuration.

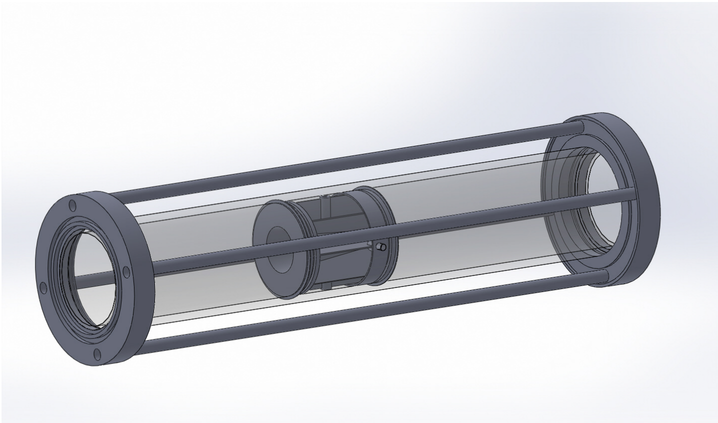

FIGURE 2.2: A model of the jet pump test section as designed by F. Dixhoorn[7].

In the test section the different designs of the jet pump can be mounted. The high speed camera and the smoke wire are not shown. Both specifics will be elaborated in Chapter 2.2.

2.2 Image Acquisition

The following chapter describes the process of acquiring the images of the flow. This involves all actions to obtain qualitative images. Choices are to be made to obtain the images. In the following chapter these choices will be discussed and in the end a summary will conclude the choices made in the visualization of flow for this thesis.

2.2.1 Light

Light is required to capture the images. This light is supplied by a LED light source shown in Figure 2.4. The PMMA tube is highly reflective, making the placement of the LED light source critical. Multiple different light locations were tested. The final choice of the test section set-up is shown in Figure 2.3. To minimize the reflections, it was decided to illuminate the tube from the open end of the resonator. The inside of the tube gets illuminated more evenly which increases detail in the smoke. However,

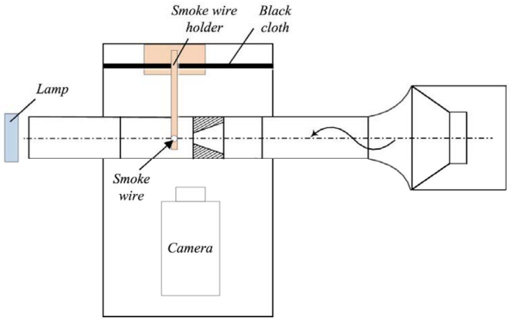

FIGURE 2.3: A schematice drawing of the test section setup with camera and light for standing wave flow visualization[34].

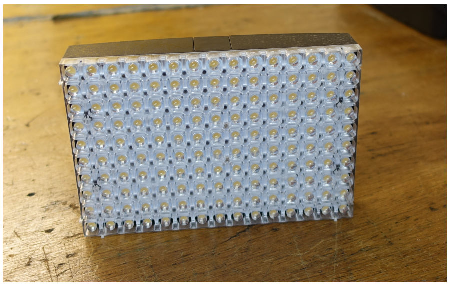

FIGURE 2.4: The LED light used to light up the set-up.

the jet pump is designed to function inside of a traveling wave thermoacoustic engine as described in Chapter 1. Therefore flow visualization with the open termination will increase understanding in the flow patterns of the “minor losses” but it will not be a true representation. Also this Tests are done with a jet pump with a black face, although this decreases reflections it also decreases the light inside the tube drastically. This is important because getting enough light in the tube improves the contrast of the image and reduces noise.

2.2.2 Camera Setup

These flow effects are high speed oscillatory effects and cannot be seen by the human eye. The frequencies of the oscillations are between $28Hz$ and $169Hz$. The high speed camera available is capable of shooting up to 1000 frames per second (fps) with the limited light in the test section. The camera is a Phantom v7.3 high-speed camera with a Nikkor 40mm lens at aperture f/3.6.

Camera Triggering A control software is used in operating the Phantom high speed camera. Within this software, it is possible to control all parameters of the camera. It shows a preview of what is to be recorded and allows for advanced image processing. With the software the camera is also triggered.

Image Extraction The images are recorded inside the internal memory of the camera. Its internal memory allows recording 8800 frames. The control software can save these images in multiple formats and is not limited to just video. To import these images in Matlab, they must first be converted in to a compatible file format, DNG.

DNG images are digital negatives, an open standard RAW file developed by Adobe, and accessible by numerous programs including Matlab while retaining their raw file quality.

2.2.3 Smoke Injection

A smoke wire is used for smoke insertion. A heating wire is vertically placed inside the tube and a smoke liquid steadily flows down while evaporating and generating smoke, shown in Figure 2.5. The amount of smoke generated depends on the material of the smoke wire, smoke liquid, the liquid flow speed and the temperature of the wire. The material chosen for the smoke wire is based on its strength, its temperature when current is applied and its diameter. An NiCr 8020 material is chosen with a diameter of 0.2 mm because of its flexibility and the range of temperatures it can withstand[34]. The wire is mounted between two Teflon plugs, that keep the smoke from leaving the PMMA tube, prevent smoke liquid flowing along the sides of the tube but more importantly keep the PMMA tube from melting. The upper plug consists of a reservoir which contains the smoke liquid and a needle to apply it to the smoke wire. The liquid flows through the needle along the smoke wire.

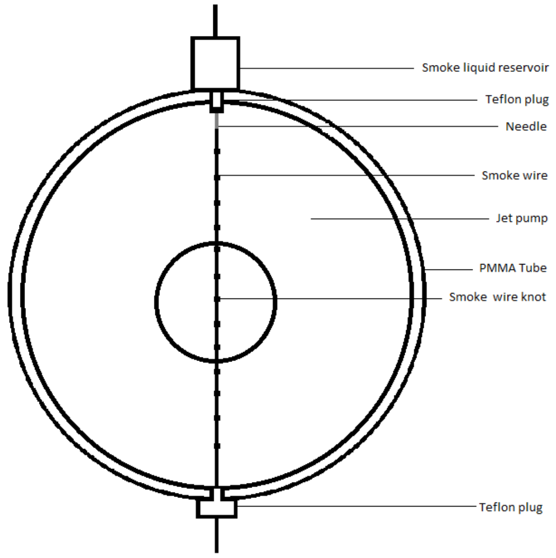

FIGURE 2.5: A schematic drawing of the smoke wire applied to the test section.

When this flows too quick there is minimal evaporation of smoke liquid, hence resulting in minimal smoke generation. This is solved by increasing the hindrance to flow of the smoke liquid along the wire by tying knots which hold small amounts of oil to evaporate. The knots are spaced 1 cm apart across the full length of the smoke wire to produce a steady injection of smoke.

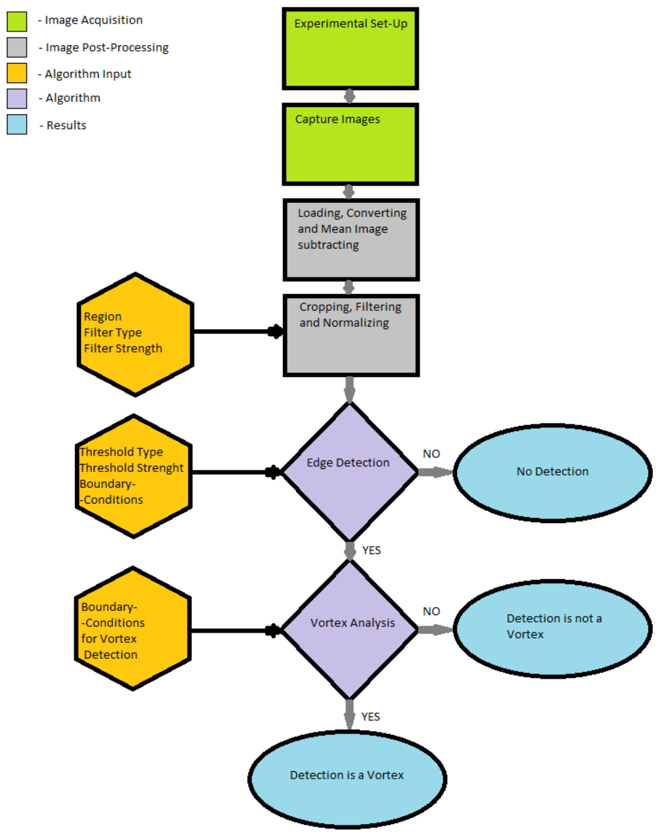

FIGURE 2.6: A flow chart showing the flow visualization process.

2.3 Image Post-Processing

There are almost 9000 images captured with each flow visualization and these images require analysis. The analysis is focused on vortex detection. Manually doing this involves measuring pixel distance between vortices in subsequent frames. This is meticulous and exhaustive work which is also prone to user induced errors. For these reasons, it is preferred to create an automated algorithm in Matlab which requires minimum user input to detect the vortices and save their paths, a flow chart of the flow visualization is shown in Figure 2.6. In the following section, the process of post-processing is discussed.

2.3.1 Vortex Detection Algorithm

The suggested algorithm needs to locate, track and measure the vortices leaving the jet pump. This algorithm, would ideally be fully automated, where importing the images is the only manual task. Realistically, it still requires parameters from the user to produce quality results(discussed in Chapter 2.4). The Matlab software has an image toolbox and there are many techniques available for image post-processing. Image post-processing

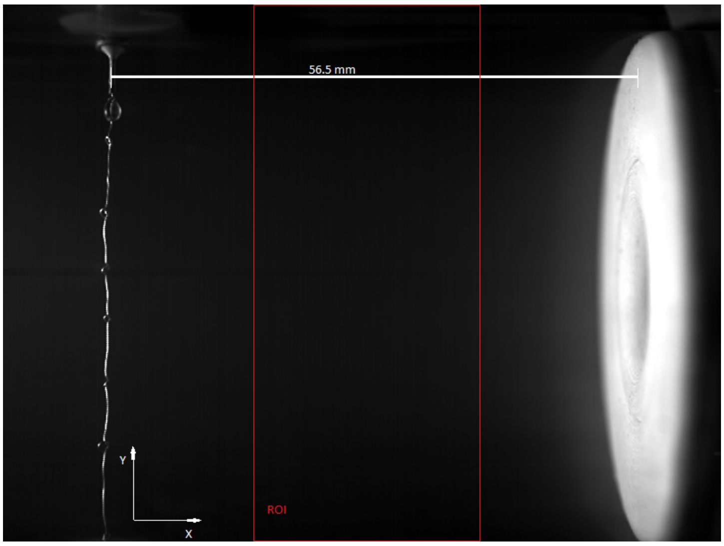

FIGURE 2.7: A schematic drawing showing the scale and the region of interest.

is a heavily researched subject and this provides many worked-out options with easy implementation.

2.3.1.1 Loading Images, Conversion and Mean Image subtraction

The selected frames go through multiple steps to create gray-scale images. The images are balanced. Balancing changes the distribution of the image data created by the camera sensor. The images then undergo a demosaicing process, this aims to create the true pixel values from the RGB values created by the Bayer image sensor in the high speed camera. The remaining step is changing the image into a gray-scale, the result is a matrix of 800×600. The length scale is determined from a sample image. The length between the nozzle of the needle and the jet pump is taking as a reference. In Figure 2.7 the length is shown and the scale derived from it is $0.0495 \, \frac{mm}{pixel}$ From the range of images loaded into Matlab, a mean image is taken. In this image all steady and consistent image content is present. This is assumed as the background of the image. If this background is subtracted, it leaves the foreground for further image processing. This is called foreground detection and is widely used to detect moving objects from static camera images. This background serves as a reference frame when subtracted. This results in higher contrast of motion between subsequent frames.

2.3.1.2 Cropping, Filtering and Normalizing

The image is cropped to focus on the region of interest(ROI). The region is shown in Figure 2.7. The size of the ROI along the X-axis is related to the frequency of the acoustic wave creating the vortices, the Y-axis is fully selected to be sure to capture the vortices. This is further elaborated in Section 2.4.1.1.

This cropped image is then filtered. Filtering is done to reduce the noise introduced by the low light situation. There are 3 filters implemented in the algorithm. These filters are chosen for their renown in image noise reduction. The following filters aim to reduce noise but remain detailed on the edges of objects. To get the desired effect of a filter it needs the input of a filter window size and a variance called standard deviation σ. Filters are applied by multiplication in the form of Equation 2.1.

$$I_B = F_{G,W} \times I_A \tag{2.1}$$

$F_{G,W}$ is the applied filter where G is a Gauss filter and W is a Wiener filter. $I_{A,B}$ are the images on which the filters are applied. The median filter cannot be included here because it uses a nonlinear method.

Gaussian Filter Is considered as the optimal linear smoothing filter. The negative contribution of frequency components in images is reduced in a controlled manner. the software implementation of the Gaussian filter uses Equation 2.2.

$$F_G(x,y) = e^{-\left(\frac{x^2+y^2}{2\sigma^2}\right)} \tag{2.2}$$

The coefficients of the image $F_G(x,y)$ are calculated with the help of Equation 2.2, the coefficients are based on the center of the image. The center size is determined with the window size and standard deviation σ input[24]. X and y are the distances from the origin in respectively horizontal and vertical direction.

Wiener Filter This linear filter tries to improve images heavily degraded by noise. It aims to restore the original image by applying a filter. The action of the filter is determined by the error between the image with corrupting noise and the filtered image[37]. In Equation 2.1 the application of the filter is shown, the error with respect to time t is shown in Equation 2.3.

$$e(t) = I_A(t+\alpha) - I_B(t) \tag{2.3}$$

The α term is the delay introduced by applying the filter, in the case of Wiener filtering $\alpha = 0$. The filtered image can also be written as Equation 2.4.

$$I_B(t) = \int_{-\infty}^{\infty} F_W(t) I_A(t+\alpha)dt \tag{2.4}$$

The error is squared and then minimized to find an optimal $F_W(t)$. This is done by solving the Wiener and Hopf equation which goes beyond the scope of this thesis[37].

Median Filter This kind of filtering is nonlinear and used for noise reduction. It is based on creating a median value of a $m \times n$ matrix. the median value is thus a result of the values from the neighboring values. The pattern of neighbors is called a window and these windows can take complex shapes for 2D median filtering. The results are a filter that has demonstrated the capability to reduce noise whilst retaining feature boundaries. Matlab implements the filter using the same method. The application of the filter could cause distorted edges as the $m \times n$ matrices which cross the edge of the images are padded with zeros[24]. These zeros cause the median values of these matrices to be off.

The result is a cropped and filtered image. The type of filter chosen is important to allow better processing in the following steps. Higher filter strength also lowers the computational load for the edge detection as there is less detail in the edges to be detected. The optimal filter for the flow visualization is discussed in Section 2.4.1.1.

To make the image values more convenient in mathematical operations and plotting, the images are normalized. The images are in 8-bit gray-scale so the values in the image range anywhere between 256 for total presence (white) and 0 for no presence at all (black). These are given more intuitive values. The values are scaled to be anywhere between 0 for black and 1 for white.

2.3.1.3 Edge Detection

The vortices in the range of images need to be segmented from the rest of the image. The grayscale images the algorithm has created can be converted into binary images with thresholding. The vortices appear to be darker then the surrounding areas. When a threshold is applied, an image with the vortex present should be segmented as a black region with white surroundings. The threshold value needs to be correct: too low and there is no detection; too high and there is over detection.

Because of the importance of the threshold, multiple methods are investigated. The following thresholding methods are selected because of their performance on comparable images in literature[29]. The best performing thresholding methods are chosen from different categories to give a good representation of the methods available.

Otsu's algorithm This method is available in Matlab within the "graythresh" function. The algorithm assumes that pixels either belong to the foreground class or background. The optimal threshold is when the overlap of the histograms from these pixels is minimal. the separated pixels belong to classes (foreground or background). The process can also be described as minimizing intra-class variance, which is defined as the weighted sum of variances of the two classes[10].

Every image has a histogram. The method assumes this histogram is divided into two by threshold t. From the histogram the probability, $\omega_i(t)$, of a pixel belonging to the background class of foreground class is determined for both parts, i, of the histogram. With the histogram, μ_i is also calculated, this term is described as the mean between two classes. the intra-class variance, $\sigma_b^2(t)$, is then calculated with Equation 2.5.

$$\sigma_b^2(t) = \omega_1(t)\omega_2(t)(\mu_1(t) - \mu_2(t))^2 \tag{2.5}$$

Finding the maxima from Equation 2.5 for $\sigma_b^2(t)$ for both parts of the histogram results in the corresponding thresholds. The desired threshold is then the average of these two.

Kittler The Kittler method is developed to create a computationally efficient method to calculating minimum error thresholding. It works on the assumption that the pixel grey level values are normally distributed[20] and can be separated for the foreground and background in two gaussian curves. A performance curve is made for correct classification between the foreground and background called the criterion function.

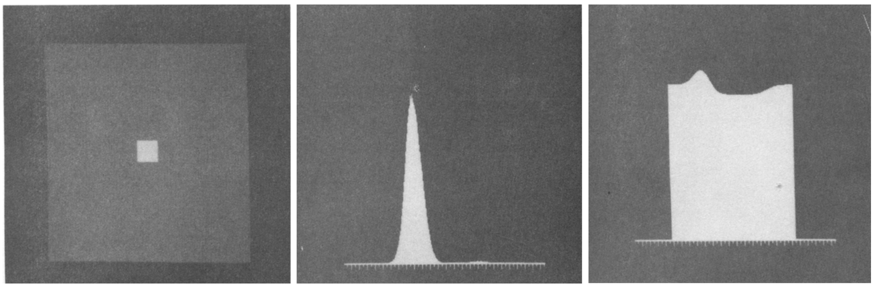

FIGURE 2.8: Left: A sample image of a grey square with black background; middle: histogram of the sample image; right: criterion function of the histogram with a clear internal minimum[20].

The criterion function, shown in Figure 2.8, is a subtle manner of finding the right threshold value. for any threshold the criterion reflects indirectly the overlap between the histograms of the foreground and background. A smaller overlap leads to better segmentation between foreground and background. So the threshold value which gives the lowest criterion value results in the optimal segmentation.

Kapur The Kapur method calculates the optimal threshold by optimizing the entropies for two different distributions of graylevels. Entropy is a statistical measure for describing the randomness of graylevels in the image. Minimizing the random gray level probability will increase the accuracy of the image's histogram. With the histogram it is possible to find the threshold which maximizes the segmentation of information between the foreground and the background[19]

Triangle A method which originated from medical image analysis. The threshold is geometrically determined from the histrogram of the pixel intensities. The maximum of the histogram is detected and a line is drawn between this maximum and the highest level of the histogram (usually 256 in 8-bit images). Now the distance between this line and the main peak in the histogram is maximized, which gives a location on the X-axis. In the research performed by G.W. Zack a factor **A** was added to this to increase segmentation. In figure 2.9 the geometrical process is shown, the threshold is also indicated[44].

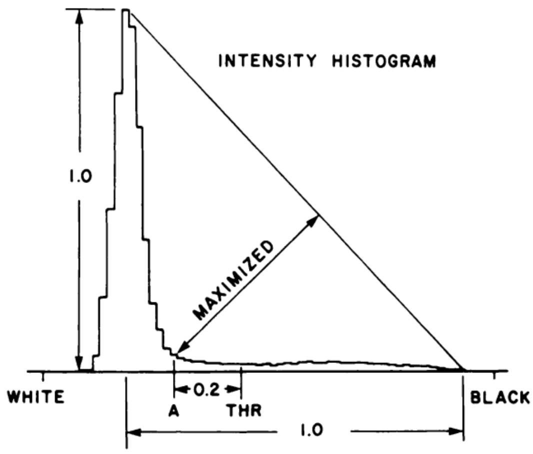

FIGURE 2.9: The geometrical process of calculating the threshold (THR)[44].

To summarize, the thresholding methods are designed to separate pixels between foreground and background. So also between relevant and irrelevant objects. All methods seem to over estimate the threshold. The threshold constantly gets set too high and to attain good separation between the images a factor is introduced to reduce the threshold level. This is undesired, as this increases the user involvement in the algorithm. After the threshold is applied, the images are binary. Matlab has built in edge detection algorithms which can detect the shapes in these binary images.

Implemented in the Matlab algorithm are some basic boundary conditions to simplify the ROI for the edge detection algorithm. There are three different types of boundary conditions applied.

- Detected regions in the top and bottom pixels of the ROI are removed from further processing. The vortices are propagating from the right to the left in the middle of the ROI. Any detected regions in the top and bottom are considered pollution.
- The left side of the ROI also neglects detected regions but for different reasons. With vortex analysis, in Chapter 2.3.1.4, the propagation speed is calculated but from the preliminary graphs it appeared vortices slowed down near the end. This effect is not expected and caused by the edge detection algorithm. As the region moves through the left side of the ROI, it is still detected which results in a lower detected speed.
- The size of the detected region, which has a minimum and a maximum.

2.3.1.4 Vortex Analysis

To improve the accuracy of the found regions and verify if they are vortices, a vortex analysis is implemented. Verifying the regions is done with more conditions. But these are specific for the properties of a vortex. The analysis runs through all detected regions to check if there are any vortices. The conditions state:

- Vortices have to propagate to the left. Any regions that is not moving left cannot be a vortex and is deleted. Whether the region is moving left, is determined by evaluating the location of the center point of the detected region. If this center point moves left in subsequent frames, the detected regions is consider a vortex.
- More detected regions have to follow after the first vortex detection. If a vortex is detected, two other vortices need to be detected in the two subsequent frames.
- A vortex can only propagate with a certain speed. To filter outliers from the detected regions a maximum speed of 10 m/s is set and a minimum speed of 0 m/s.

When a detected vortex fulfills these conditions, it is called a trace. These traces are equal or longer than 3 detections in a row. From these traces the propagation speed is calculated by differentiating the location of subsequent center points with respect to the time passed.

2.3.2 Alternative Image Analysis Tools

There are many alternative analytically tools to our disposal. The following section will give a short description of promising techniques capable of correlating two images. The current Matlab algorithm can detect vortices in frames but does not use any information available from subsequent frames. This is a highly discussed topic in literature in medical or surveillance fields of research. These research fields mainly use it to map images on top of each other using subsequent image information, but that does not mean the methods can be repurposed to benefit vortex detection and vortex propagation speed calculations.

2.3.2.1 Image Registration

The following section describes the main algorithm of image correlation. The following techniques all use this algorithm with only small differences. Image correlation algorithms are used to find correspondences between images. These correspondences can be found by using multiple techniques with various characteristics. The characteristics range from landmark positions, contours, surfaces, and volume of intensity plots[17]. The algorithms try to achieve smooth transformation of the geometrically altered image Z_M (often referred to as a moved image) to the reference image Z_R. The transformation is denoted by matrix $\mathbf{T}(x, y)$ so that $Z_M(\mathbf{T}(x, y))$ is as close to the reference image as possible[41].

Intensity Based Image Registration For intensity based image registration (IBIR), the geometrical transformation $\mathbf{T}$ is created by best matching Z_M and Z_R on their similar/dissimilar observed intensities. Applying the transformation matrix to Z_M allows for precision mapping on top of the reference image, establishing a point-by-point correspondence. IBIR can achieve automatic mapping without any prior input about shapes or features in the reference image. This saves a time consuming and calculation heavy task for the computer doing the registration.

IBIR can be adapted easily, allowing it to detect vortices based on their generated intensities, or lack there of. Lets assume frame **A** contains a vortex, the subsequent frame **B** also contains a vortex. The IBIR technique let us match up these vortices and calculate the geometric transformation matrix **T**. This matrix **T** contains the translation information of the image from where the displacement of the vortex can be derived. This displacement should be more accurate than with the edge detection method because it matches the vortex on **A** with the vortex on frame **B** both in x and y coordinates. Also the highest intesities are centered on each other which generates a more precise center point of the vortex.

Optimal Mass Preservation Based Image Registration This is similar image registration as the IBIR technique but to calculate the transformation matrix **T** it uses the optimal mass transport theory developed by G. Monge[23] and improved by Kantorovich[18], and known as the Monge-Kantorovich transportation problem[47]. It is a study in the optimization of transportation and allocation of resources. It works under the assumption of a constant mass during the process of transportation. The theory behind this goes beyond the scope of this report. Understanding its application to image registration is however, will be discussed in the following

The same frames are taking as described above,**A** and **B**, and we assume each of them have a positive mass density function $\mu_{A,B}$. The assumption that the total amount of mass per image is the same is made as well. This gives Equation 2.6 for the Jacobian transformation when u is used to map frame **A** to frame **B**.

$$\mu_A = |Du|\, \mu_B \circ u \tag{2.6}$$

$|Du|$ is the determinant of the Jacobian of u and $\circ$ is the composition of functions. We are now interested in finding a map u which changes the mass preserving mapping minimally to find the closest match. Here the Kantorovich-Wasserstein penalty L^2 is introduced, this places a penalty on the distance the map u has to move each pixel, weighted by the pixels intensity. This results in a distribution of materials which is forced to be frame **B**. This leaves the calculation of the "optimal" map of frame **A** on **B**, this is a heavy computational step but also one with substantial literature research with multiple strategies to reduce the computational load[46]. With this "optimal" map it is possible to determine the translation of the vortex and use this to calculate is propagation speed.

Continuous-Field Image-Correlation Continuous-field image-correlation (CFICV) uses regions instead of pixel intensity values to compare image Z_M with image Z_R[11]. Simultaneously the transformation matrix **T** is used to minimize the cost function described in Equation 2.7

$$\jmath = \int_\Omega [Z_M T - Z_R]^2 d\Omega \rightarrow min \tag{2.7}$$

Ω is the correlation domain. This is the boundary region limited to the size of the image but commonly split up in smaller regions to increase accuracy. Minimizing the cost function 2.7 is done by iteration until matrix **T** achieves the best mapping.

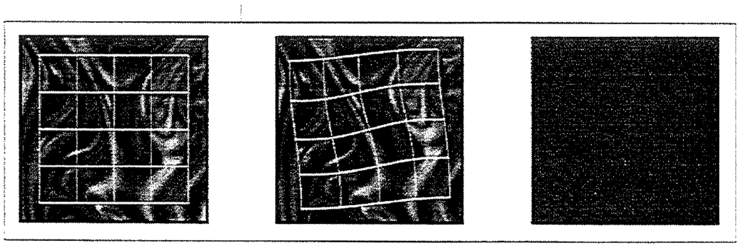

FIGURE 2.10: With the continuous-field image-correlation these are the results, from left to right: Z_R,Z_M and $Z_M T - Z_R$[11].

In Figure 2.10 we can see examples of the procedure. From the translations of those cubes and its center points we can calculate vectors for velocity and vorticity.

Tracking of Non-Rigid Objects This is not necessarily a method of image registration but an alternative for edge detection. This technique works by specifying a template of the object of interest. The process applies a parametric transformation to allow variability in the template shape. There are promising classical deformable template based tracking algorithms developed but they function in similar manners[45]. The difference is the assumptions the algorithms make about the object of interest. Assumptions can be made about the shape, the shape change and to what degree of change[25]. Also the location where the shape is detected can be assumed either anywhere in the image or a certain region[15]. The algorithms are self learning to a point but still need basic input about the object of interest. In Figure 2.11 an example of non-rigid detection is shown[25]. The final decision on where the object of interest is detected depends on a voting stage, where in this case there were more votes for the right detection.

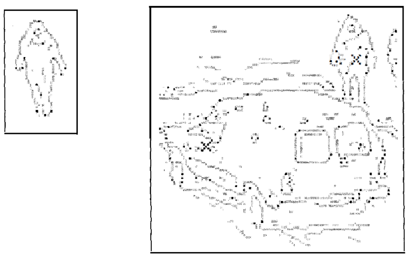

FIGURE 2.11: The left images shows the learned shaped and in the right image it shows the detected shape in the larger form. The crosses note the detected places before voting on which is better matching[25].

The vortex has a particular shape different from the background of the footage. The shape can be learned or supplied by the user to be implemented into one of the tracking algorithms. As soon as the vortices are detected and tracked the calculation of the speed is a derivative of the displacement.

Salient Motion Object Detection Salient motion means the important or interesting motion in recorded footage as opposed to non-salient motion. In the case of this thesis, the vortices are considered as salient motion while all other movement is non-salient. Salient motion detection works by performing these steps[40][33]

- Step 1 - Calculate the region of change, which is calculated by subtracting subsequent images and applying a threshold to extract the moving pixels
- Step 2 - The optical flow, also known as a 2D motion field, of the pixels is calculated from frame-to-frame.
- Step 3 - The direction of the pixel motion inside the region of change is determined. The direction is sorted in X and Y direction.
- Step 4 - Pixels which continually move in a constant direction are used as seed pixels. The neighbor pixels are also checked until it grows in a $N \times N$ region of pixels moving in the same direction. Also described as the salience field.
- Step 5 - Objects with salient motion are finally detected when the information form the previous steps is combined.

The result is a salient object, the steps of detecting salient motion can be seen in Figure 2.12.

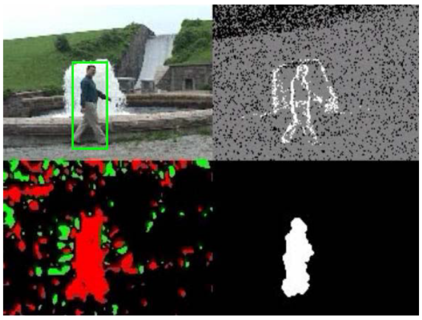

FIGURE 2.12: Showing the steps of detecting salient motion. Left top: original image; right top: difference image; left bottom: X-Component of the flow; right bottom: final detected salient object[33].

The result is a black and white image where with edge detection the object can be tracked. The tracked regions can undergo vortex propagation speed calculations.

2.3.2.2 Summary

Some of these methods calculate the vortex propagation speed with the same techniques(IBIR, Optimal Mass Preservation and CFICV). There are subtle differences in the manner of calculating the transformation matrix. After this matrix is found the algorithm for the vortex tracking would be the same. CFICV method is less useful for the calculation of vortex speed because it looks in multiple regions spread over the image and focuses on small changes within those regions. This would make it an ineffective method for vortex tracing but suitable for displacement velocity calculation. These methods do have the advantage of tracking regardless of knowing which shape to track as opposed to the non-rigid object tracking. Therefore this method seems ineffective. Salient motion tracking seems the most promising method. The vortices move in a constant direction from right to left which is the ideal movement to apply this method. The implementation in Matlab is not straight forward. It requires an in-depth knowledge about image/video manipulation and mathematics. However the computational load is average compared with the other methods. Also taking into account the pixel by pixel calculations involved in this method.

2.4 Process Validation

The created algorithm manages to track the vortices, plot their paths and calculate their speeds. However, the accuracy of the acquired data is yet unknown. The following section gives insight in the accuracy of the algorithm. A method will be introduced for finding the parameters which dominate the algorithms accuracy.

2.4.1 Statistical Analysis

The algorithms accuracy will be estimated by commonly used methods in statistics. These methods are often used in image post-processing fields to justify the use of certain methods. For this reason the statistical tools will be applied on the Matlab algorithms to justify using it to detect vortices.

A total of 500 images are imported into the algorithm. The investigated parameters are: filter type, filter strength, threshold method, threshold multiplier, boundary conditions for edge detection, boundary conditions for vortex detection and region of interest size. The influence of these parameters is assessed with a ROC-curve, the imported frames are sampled to find the values required to create these curves.

2.4.1.1 Receiver Operating Characteristic Curves

The ROC-curve is used in medical fields to determine whether a patient will need hospitalization or will benefit from treatment[13]. The method is an objective tool in making

Contingency Matrix

Positive Test Outcome	True: Vortex undetected where a vortex is present	False: Vortex undetected where no vortex is
Negative Test Outcome	False: Vortex undetected where a vortex is present	True: Vortex undetected where no vortex is

TABLE 2.1: Table summarizing the results from the image post-processing in statistical terms.

these decisions. The method compares two Gaussian distributions, one for negative cases of the algorithm and one for positive cases. The lesser these distributions overlap the better the separation is between good results and bad results. An example of a ROC-curve is shown in Figure 2.13.

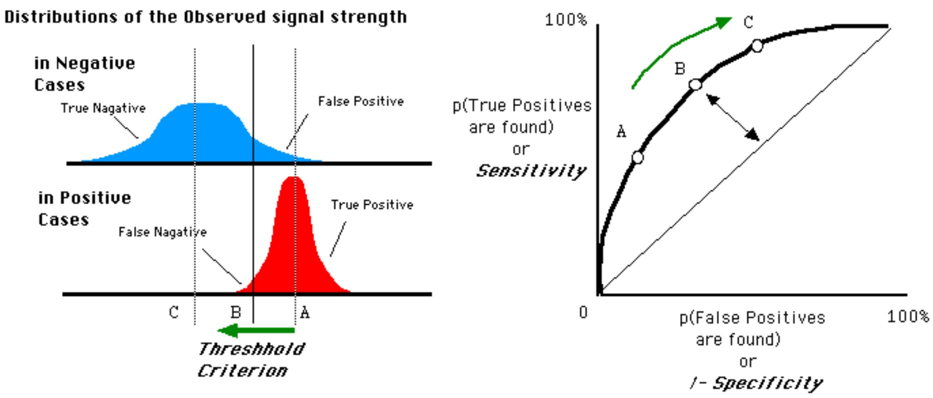

FIGURE 2.13: An example of a ROC-curve with the distributions for negative and positive cases[38].

On the x axis $1-$**specificity** is denoted, also known as the false positive rate (FPR). This can be written as FPR = FP/(FP+TN), where FP are false positives and TN are true negatives. The y axis is the **sensitivity** or the true positive rate (TPR). Written as TPR = TP/(TP+FN), where TP are the true positives and FN are the false negatives. The ideal shape of the ROC-curve would keep close to the left side and only separate for higher values on the y axis.

The different outcomes of the process, shown in Figure 2.6, require reformatting in the terms FP, TP, FN and TN(this is shown in Table 2.1).

These outcomes are acquired by sampling the imported images. The images are manually controlled to see if the detection made the correct conclusions. To get the necessary accuracy of the outcomes there needs to be a certain amount of sampled images. Equation 2.8 is used to determine the number of images to sample, also known as sample size N_{SS}. To achieve an accuracy of 95% the confidence level is $Z = 1.96$, the Z is a

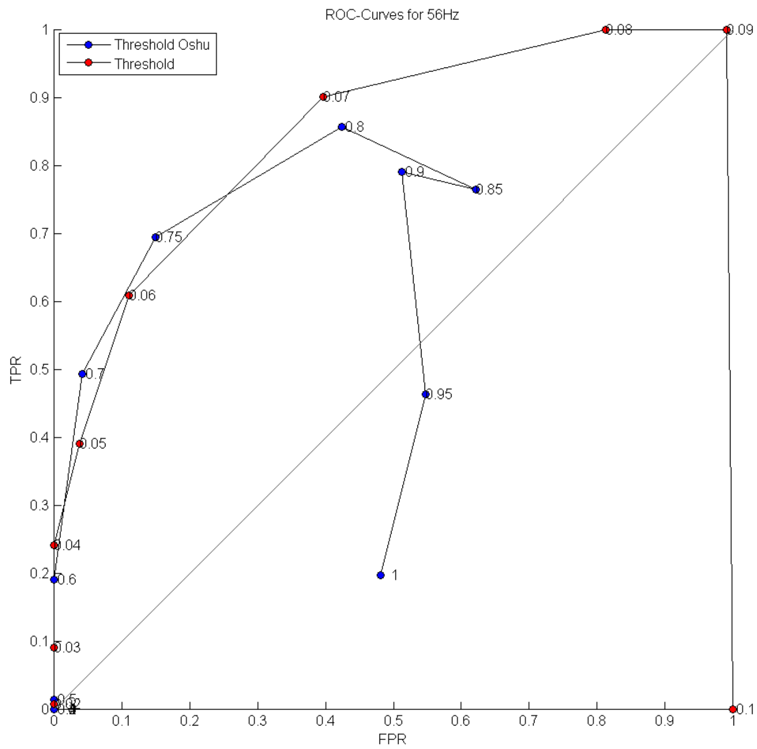

FIGURE 2.14: An example of a ROC-curve with the threshold data from Othu's method and the true threshold values for 56Hz frequency.

term from normal distributions. p are the chances for the expected results, $p = 50\%$ is used to give the largest sample size. On the accuracy a margin of error is added, this is the amount of error tolerable for taking the sample. In the case for the ROC-curves the desired accuracy is 95% with only 5% deviation.

$$N_{SS} = N_{PS}\frac{Z^2\, p(1-p)}{Z^2\, p(1-p) + (N_{PS}-1)\, E^2} \tag{2.8}$$

So to achieve that accuracy it is necessary to sample 218 images. So for every plot point on the ROC-curve 218 images are sampled to find the corresponding TPR and FPR. ROC-curves are created for the input variables of the vortex tracing algorithm for three different frequencies(28Hz, 56Hz and 80Hz), shown in Figure 2.6. The vortex decision step will be neglected in the ROC-curve. This decision is made because if a region is positively detected it could be neglected by the vortex analysis step because it does not comply with those conditions. If the vortex analysis step would be included this would change the influence of the variables for the edge detection step. The found variables might work for the vortex analysis step but are not beneficial for the overall algorithm. This is due to inconsistency with the decisions for TP, FP, TN and FN. A TP for the edge detection can be a FP for the vortex analysis if the detection does not comply as stated above.

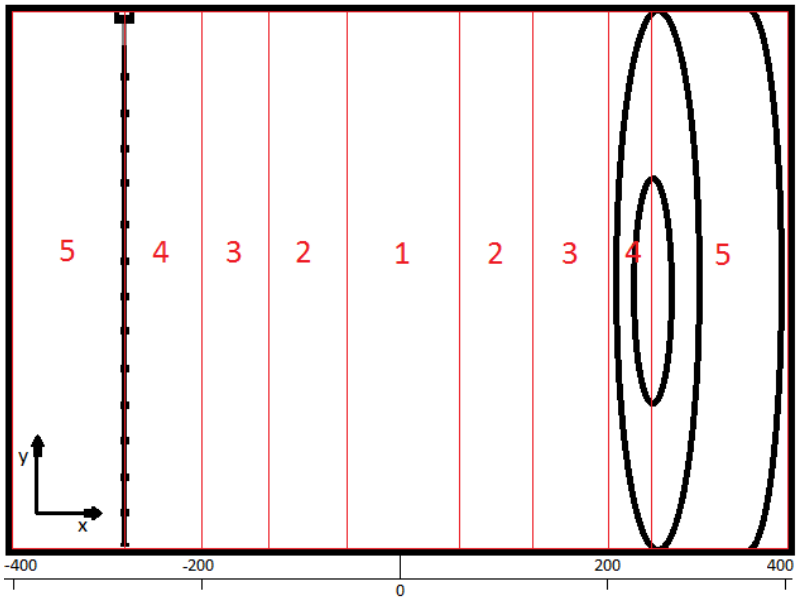

FIGURE 2.15: A schematic of the size of the Region of Interest (ROI) which is varied in the x-direction.

In Figure 2.14 a typical ROC-curve is shown. The other ROC-curves are added in Appendix A.

Thresholds In Figure 2.14 the effect of the boundary conditions is clearly visible as the decrease in TP comes earlier. The optimal value is different for each frequency but seems to be significantly higher for higher frequencies. It varies from 0.04 for 28Hz, 0.06 for 56Hz and 0.45 for 80Hz.

Filters From the ROC-curve it becomes clear that Wiener filters are not as effective as the Gauss filter. This could be explained by the different focus of the filters. The Wiener filter focuses more on edges between object and the Gauss filter is smoothing of the whole image. A lower filter standard deviation seems to work better for the lower frequency acoustic waves.

Region of Interest The ROC-curve shows that if the ROI increases in size, the size of the ROI is varied in the x-direction as shown in Figure 2.15, the performance of the lower frequencies is better while the higher frequency performance is less. Higher frequency acoustic waves create more vortices. When the ROI size is increased, there start to be more vortices in one frame and this results in faulty center points and thus wrong tracing.

Variable	28Hz	56Hz	80Hz
Threshold	0.75	0.75	0.9
True Threshold	0.04	0.06	0.45
Filter	Gauss $\sigma = 5$	Gauss $\sigma = 5$	Gauss $\sigma = 10$
Region of Interest	3	2	1
Boundary Conditions	X: 10 Y: 50	X: 10 Y: 50	X: 10 Y: 50
Minimal and Maximal Area	Min: 50 Max: 150	Min: 50 Max: 150	Min: 25 Max: 150

TABLE 2.2: Summary of the optimal values used for the variables to run the vortex detection algorithm.

Boundary Conditions The influence of this variable is inconsequential, the detected points in the ROC-curve are scattered in a small region. When unrealistic values are chosen though, the performance goes down. This proves that this variable does not contribute to the algorithm but when the wrong value is chosen it can corrupt results. The boundary condition on the left side of the ROI was not implemented to increase the performance of the detection but of the propagation speed.

Minimal and Maximal Area The minimal area proves to be an important variable. The maximal area influence increases for higher frequencies. While the data points for the maximal area are calculated the minimal area was kept constant at $50^2 px$ which can be seen for the lower frequencies. The minimal area however, proves that using a larger area is better for lower frequency acoustic wave because the vortices are larger then.

2.4.2 Optimal Input of the Algorithm

From the ROC-curves the optimal settings are deduced for using the algorithm. Table 2.2 gives a summary of the values used to create the results in Chapter 3.

2.4.3 Accuracy

The accuracy is related to the FPR and the TPR. A higher TPR means more TP results which is desired. The opposite is true for the FPR, the optimal algorithm should detect the least amount of FP. The FPR and TPR for the optimal settings is shown in Table 2.3.

	28Hz	56Hz	80Hz
TPR	0.7407	0.7159	0.7006
FPR	0.276	0.1385	0.2951

Table 2.3: FPR and TPR of the optimal algorithm settings for three frequencies.

So the accuracy of the algorithm is best for the 56Hz acoustic sound waves. There the algorithm detects the most vortices combined with the low FPR achieves the goals of the algorithm. For the other frequencies the FPR is too high, there over 25% of the detections are FP.

2.4.4 False Positive Rate Problem

When a high frequency acoustic sound wave creates vortices there is the possibility that two vortices are in the same region of interest (ROI). In a situation where a vortex leaves the left edge of the ROI and a new vortex enters on the right side, there is no frame where there are no vortices. This causes problems for the ROC-curves, more precisely for the false positive rate, Equation 2.9.

$$FPR = \frac{FP}{FP + TN} \tag{2.9}$$

In the situation with no frames without vortices, the number of true negatives, TN, would be zero. So as soon as the algorithm detects its first false positive, FP, the $FPR = 1$ and this changes the interpretation of the ROC-curve. This is a special situation but it applies in any case with few TN and makes the reliability of the ROC-curve a discussion topic. It would mean that for higher frequencies the results of the ROC-curve cannot be trusted because of the lack of TN.

Chapter 3

Results

In the following chapter the results will be presented. The intermediate steps of the algorithm will be shown. The steps are compared with the raw image to clearly show the contribution of each step to the final detection.

This section shows the preparation of the image before thresholding and edge detection can be applied. Figure 3.1 shows the foreground detection method, explained in Chapter 2.3.1.1. The right image contains the foreground information. The mean image contains the smoke wire and the jet pump as well as any reflections and other constant contents. This technique proves to be very useful. The importance of image quality is diminished due to the efficiency of the foreground detection method. It shows that the algorithm is capable of creating qualitative images even if there is pollution in the image, as long as this is constant. Creating a black jet pump or a black background seems less important as the algorithm is able to remove this from the image.

Due to the low light situation, the created noise was indistinguishable from the smoke displacement. Noise made analyzing the vortices manually difficult as the edges of the vortex could not be accurately determined. Noise was battled with the increase of light in

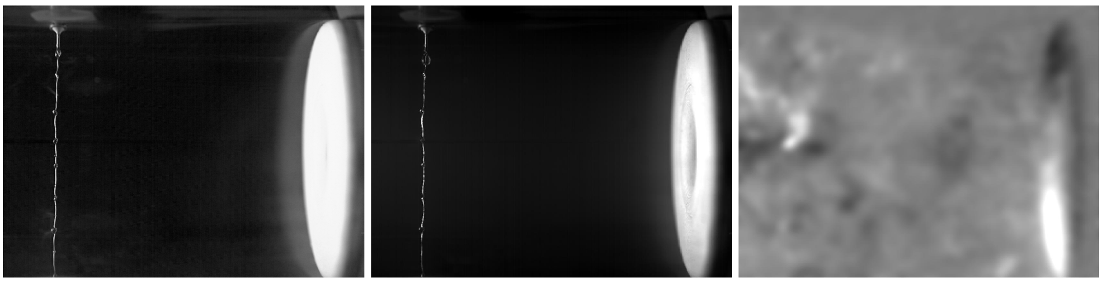

FIGURE 3.1: The subtraction of a mean image and the result it gives. Left: raw Image of the first frame; Middle: mean image created from a 500 image range; Right: subtracted image and normalized to show foreground information.

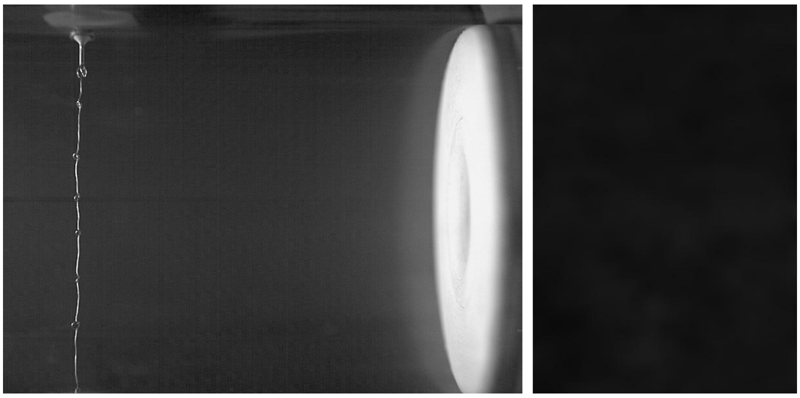

FIGURE 3.2: This figure shows the improvement of filtering, cropping and normalizing. Left: raw image, noise is present; Right: mean subtracted, cropped, normalized and filtered image ready for thresholding.

the set-up, but due to limitation of the light placement, noise was only slightly reduced. The left image in Figure 3.2 shows an average presence of noise.

The image on the right in Figure 3.2 is made after foreground detection, cropping, normalizing and filtering. This is done with a Gauss filter with standard deviation $\sigma = 5$. The image has more contrast than the right image in Figure 3.1 because of the normalization and the noise filtered out by smoothing the image. These are all the steps performed before the algorithm applies thresholding and edge detection.

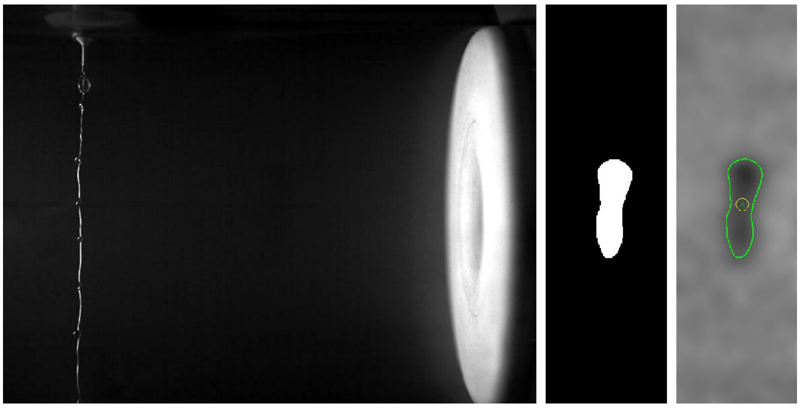

FIGURE 3.3: An identical frame before and after the vortex tracing algorithm is applied. Left: frame with vortex present; middle: frame after post-processing steps and thresholding; Right: edge detection finds region, region fulfills boundary conditions and could be considered a vortex.

To give an indication of the quality of the algorithm, the left image in Figure 3.3 shows a vortex in the middle of the image. This vortex is tough to spot. The middle image is the binary image created by thresholding after all the steps above are also performed. The binary image now shows a clear detection which could be a vortex. The edge detection creates the image on the right. It creates a contour and marks it with a yellow center point.

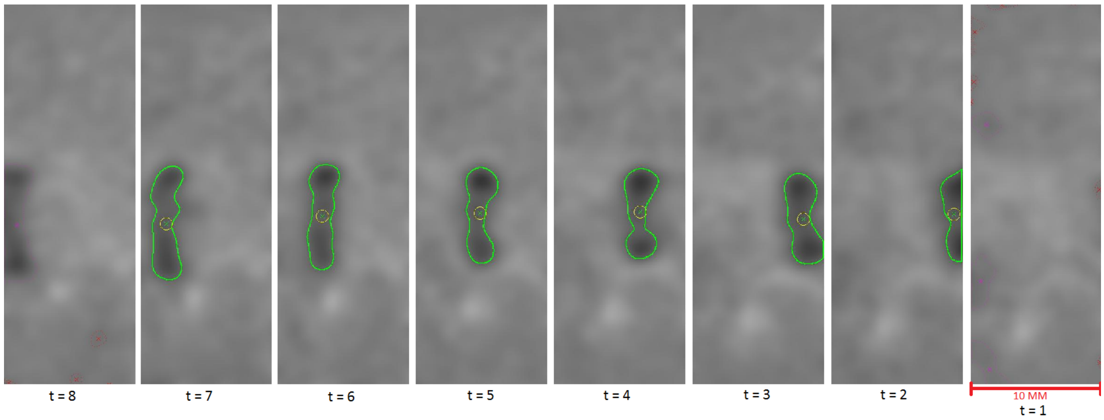

FIGURE 3.4: From right to left these are multiple detections put together to be a vortex. The acoustic sound wave is 80Hz and between each t there is $1/1000s$. This trace is used for further calculations.

This detection is not necessarily a vortex, this has to be determined with the vortex analysis. Only when this detection fulfills the conditions described in Chapter 2.3.1.4, is it assumed to be a vortex.

A detection which fulfills the conditions to be a vortex is shown in Figure 3.4. The leftmost image shows a purple detection, this is when one of the boundary conditions is broken, in this case the detection crosses the left side boundary. In the rightmost image there is a red detection. This detection breaks multiple boundary conditions.

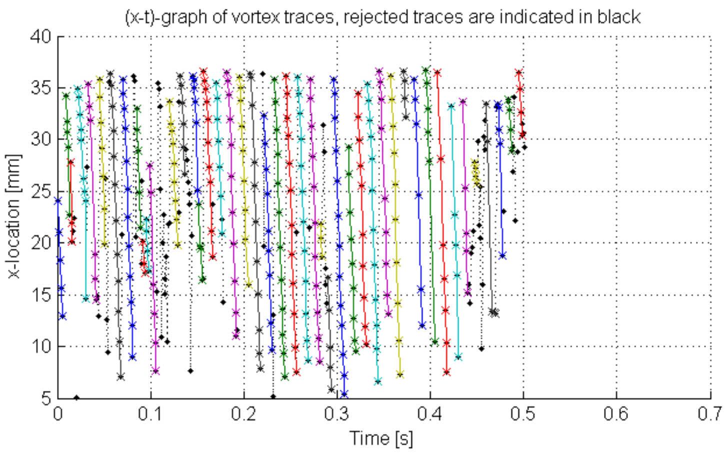

FIGURE 3.5: A graph with all traces of three detections or more at $80Hz$. The x location should be read in reverse as the origin is placed on the left side of the region of interest.

When a batch of images is analyzed by the algorithm, it creates Figure 3.5. There are 500 images analyzed of 80Hz by the algorithm which at 1000 frames per second gives 0.5 seconds worth of footage. Theoretically there should be 40 vortices traced. In reality the algorithm found 43 traces and rejected 15 found regions with the conditions of vortices.

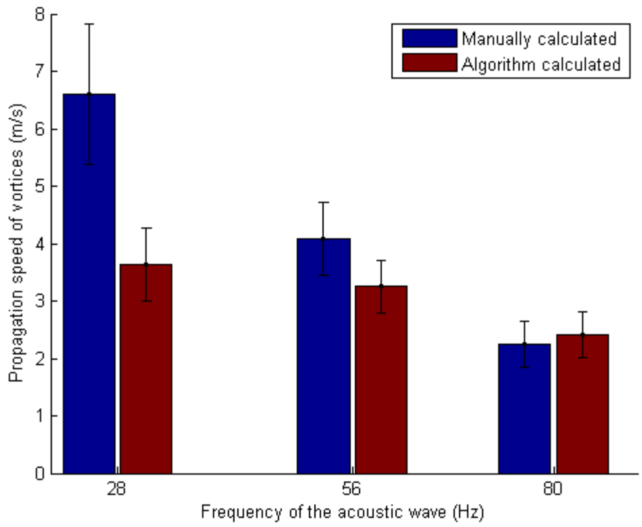

Figure 3.6: A Bar chart showing the manually calculated vortex speed and the speed calculated by the algorithm.

The propagation speed calculations are shown in Figure 3.6. There seems to be a difference between the propagation speed calculations done manually or done by the algorithm. The manually calculated speeds are higher for lower frequencies and decreases when the frequency gets higher. The trend is the same for both calculations methods but the decrease is more rapid for the manual calculations. The averages for the algorithm speed calculations are taken from the traces found for the different frequencies.

The results differ vastly per frequency, and are dependent on many variables. Not all variables are from the algorithm: the lighting, the amount of smoke in the PMMA tube are equally important for the algorithm to achieve accurate results. The lighting should be as constant as possible for the threshold method to calculate the value better. If the smoke is dispersed equally inside the PMMA tube the vortices appear with more contrast compared to any other distortions in the smoke.

The results are not always accurate and the algorithm has some errors. In figure 3.7 examples of the errors are shown. The errors lead to missed vortices, faulty traces or no traces at all. The errors are sorted into 4 main categories.

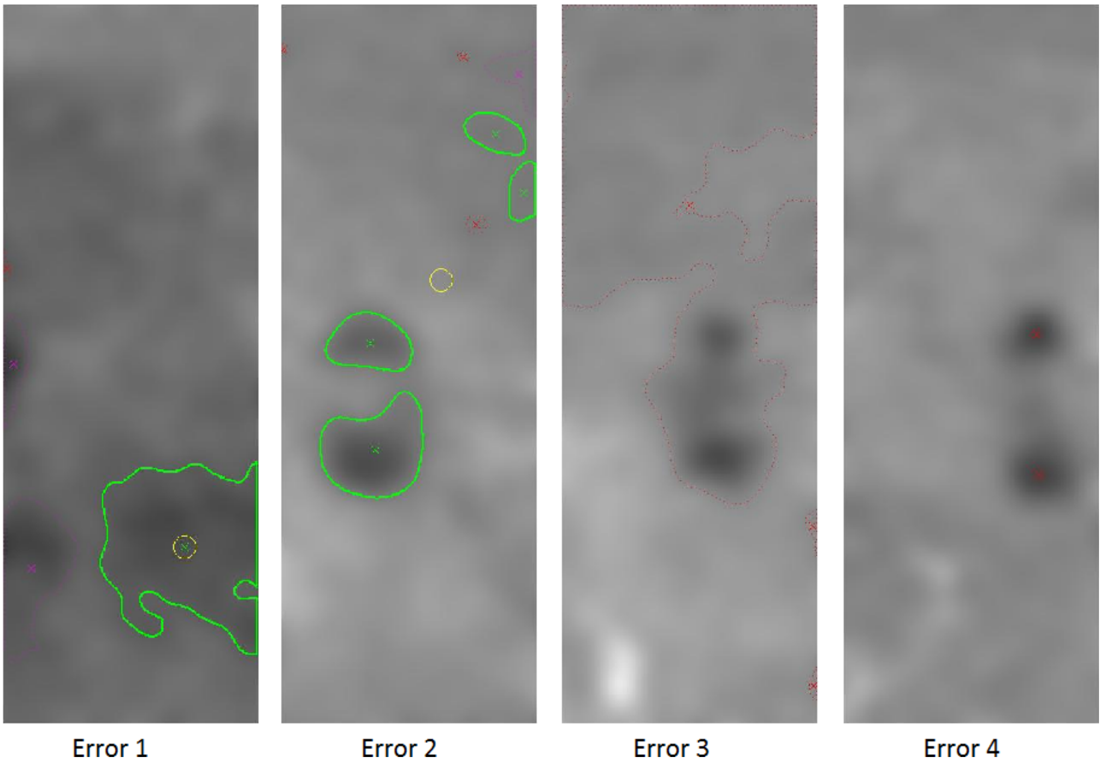

Figure 3.7: From left to right, the four types of error. Error 1: incorrect detection; Error 2: multiple detections; Error 3: over detection; Error 4: under detection.

Error 1 - Incorrect Detection An incorrect detection is described as a detection which fulfills all boundary conditions but does not contain a vortex. These errors are recorded as found regions but when the conditions for vortices are applied, the incorrectly detected regions can be be neglected from further processing. This error happens when the maximum area is set too large, and the boundaries too small.

Error 2 - Multiple Detections When multiple regions are detected the algorithm is not able to place the center point in the middle for the vortex because it is not able to determine which it is. The center point is placed in the middle for all found regions. So the center point is average between found regions. When multiple regions are found the center point gives invalid data to the vector analysis algorithm. This could cause non-vortices to be determined as vortices and vice versa.

The second issue with the center point is caused by the shape of the vortex. From this camera angle the 2D images cause the vortex to be two dark circles and a slightly lighter grey connecting them. The edge detection therefore sometimes detects two circles, one of the two circles or both circles connected. This changes the location of the center point with respect to the y axis in the region of interest

The misplacing of the center point causes deviation in the calculated propagation speeds. The propagation speeds are separated in x and y direction. For the propagation speed in the x direction, the misplacing causes the speed to increase or decrease drastically. This creates a large standard deviation of the speed and makes these results unusable for any conclusions. The propagation speed in y direction should be close to zero because the vortices move left to right with little to no up or downwards motion. The calculated propagation speeds are spread between 0 m/s and 20 m/s. This seems to be caused by the second issue of the center point, between subsequent frames the center point can jump between any detected region of the vortex. The sudden jump gives rise to the physically improbable propagation speeds.

Multiple regions are found when the threshold is set too high in combination with a lot of disturbance in the smoke. The region of interest (ROI) is also important because multiple detections can occur when the ROI is too large for higher frequencies. Then before one vortex has propagated fully to the left another is already entering from the right side of the ROI. The solution would be averaging the center point between found regions which are close to one and another. This would reduce the inaccuracy introduced by this error.

Error 3 - Over Detection When the threshold is set too high the segmentation between foreground and background decreases. This results in a detection that is too large. The boundary conditions then cause the detection to be neglected. Over detection causes missed vortices.

Error 4 - Under Detection This error is caused by the same reasons as error 3. The threshold in this case is too low, so the segmentation between the foreground and background is not large enough. The regions are then too small to fulfill the boundary condition of the area of the vortex. The effects of the error are similar to error 3.

Chapter 4

Conclusion and Recommendations

4.1 Conclusion

An algorithm was created which detects and traces vortices in the near flow field of a jet pump. This algorithm has adjustable options for filtering and thresholding. The current algorithm is able to find a vortex where the human eye cannot. The focus on the patterns detected with flow visualization is only minimal for this thesis, but the foundation has been built for automatic analysis of flow visualization.

However, the algorithm does not come without its flaws. The influence of the variables differs vastly. The threshold and the filter choice are a large factor in getting the desired vortex detection. If these variables are off they have the potential to ruin the edge detection. For thresholding, the automatic methods seem to overestimate the value which leads to over detection. The size of the region of interest should be smaller for situations with higher frequencies, because the vortices travel less far, are smaller and slower in those situations but also for the false positive rate with ROC-curve analysis. The boundary conditions for the edges do not seem to contribute to the algorithm but the ROC-curves from the threshold indicate they do influence the end results of the vortex detection. The boundary condition for the minimum and maximum area of detection also depends on the frequency. The lower frequency vortices are larger, faster and disturb the surroundings in the tube. The minimum area of detection should be increased because of that. The maximum area of detection does not influence the quality of the algorithm.

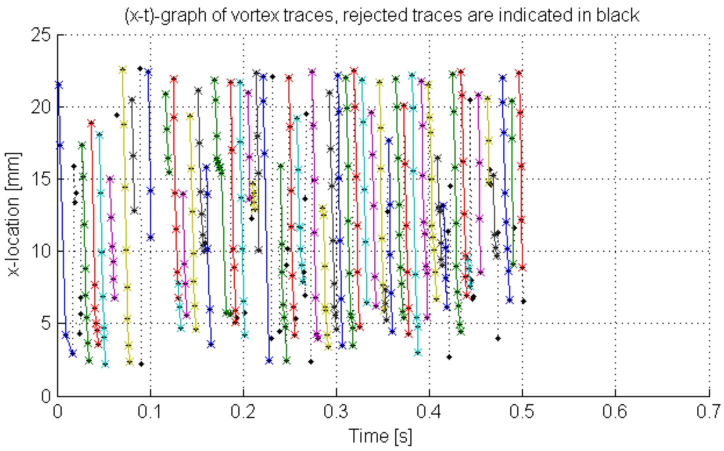

FIGURE 4.1: A graph with all traces of three detections or more at $113Hz$ after three attempts of running the algorithm. The x location should be read in reverse as the origin is placed on the left side of the region of interest

The dependency of these variables causes the algorithm to require a substantial input from the operator. The input of the algorithm requires tacit knowledge to acquire qualitative results. The algorithm does improve the speed of the analysis, a trail has been performed with a frequency of $113Hz$ to find the amount of tries it takes to find the desired vortex traces. Within three tries the traces in Figure 4.1 were found that achieve the required accuracy.

4.2 Recommendations

During the research of this thesis there were some improvements that could be applied to achieve better flow visualization of the flow field. These improvements could not be implemented in the timescale of this thesis and are recommendations if the research were to continue.

4.2.1 Flow Visualization Improvements

The recommendations regarding the low light situation of the set-up and the undesired reflections seem to be less critical now. In the process of the creation of the algorithm, it came to light that the possibilities of improving the image with the algorithm are promising. The background and reflection of the PMMA tube are removable with tools in the algorithm. For these reasons the focus can be shifted towards the creation of more interesting footage.

Many improvements in flow visualizations have been made by the predecessors. Their recommendations led to the high speed camera and the new method of smoke injection. Another recommendation which keeps returning is the use of a powerful laser. With such a laser and a high speed camera the flow patterns can be visualized in a 2D plane. The current red 5mW laser does not have enough power to create enough light to use the high speed camera at a 1000 frames per second. PIV techniques use laser up to 60mW, these lasers are also colored green which is beneficial for the camera sensor due to the Bayer layout. Though implementing this laser would involve complete rebuilding of the set-up as precautions have to be taken to protect the researchers from this class 3 laser. Applying this laser will allow the use of both smoke and PIV as flow visualization techniques, PIV has proved a fruitful technique for displacement analysis with image cross correlation. The use of these methods could improve the quality of the flow visualizations. Despite the costs and risks of implementing this laser, it could provide new insights in the flow field near the jet pump.

4.2.2 Algorithm Improvements

The algorithm is flexible and can be improved when new techniques are found in image post-processing. The options for improvement described in Chapter 2.3.2 could improve the analysis of the image. Especially the salient motion technique, which could be used instead of edge detection and thresholding. The technique is not computationally heavy despite the iteration calculations on pixels. Due to its mathematical nature the technique should be implementable in the algorithm with certain ease.

The current variables in the algorithm are influencing the quality of the outcome significantly. Choosing the wrong input values will result in trivial traces if there are any. To improve the robustness of the algorithm it should be a goal to decrease the involvement of the user. The variables should be determined automatically and only dependent on data from the flow visualizations. This is especially the case for the filter and threshold. These two variables should learn from analyzed images and then verified with a certain quality index. The threshold implementation should be improved to yield more constant results for different images.

The statistical analysis of the algorithm is done up to the edge detection step in Figure 2.6. The vortex analysis step is not yet checked due to the inconsistent results of true positive, true negative, false positive and false negative statements. With these inconsistent results the ROC-curves would be trivial. A method has to be developed to asses the accuracy of the complete algorithm.

The algorithm shows a lot of promise. It opens up possibilities for further image processing. The current algorithm only focuses on the vortices created by "minor losses" but there are more dissipative effects. The oscillatory displacement of the flow field could also use an algorithm to calculate the displacement velocity. The continuous-field image-correlation discussed in Chapter 2.3.2 already shows some promise in calculating vorticity and velocity of small displacements. With this method it could be possible to visualize the flow field and find the displacement speeds all through the region of interest.

Appendix A

ROC-curves

The ROC-curves referred to in Chapter 2.

Threshold There are two ROC-curves made for the threshold. Figure A.1 is created using Otsu's thresholding method, The value shown in the graph is the factor used to decrease the overestimated value from Otsu's method. The inconsistent shape is caused by the boundary conditions, these conditions remove detections in such a way

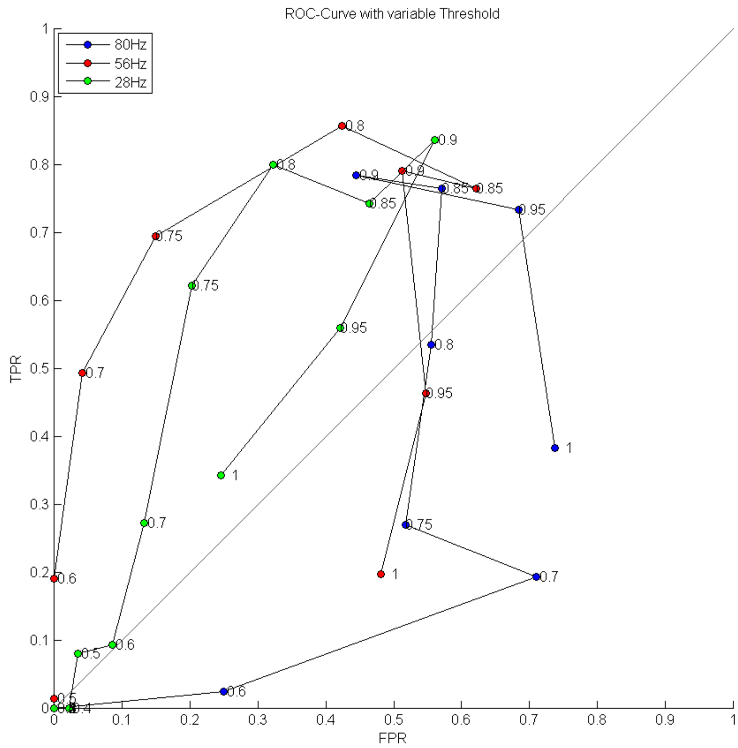

FIGURE A.1: ROC-Curve for the threshold value using the Otsu method (graythresh in Matlab).

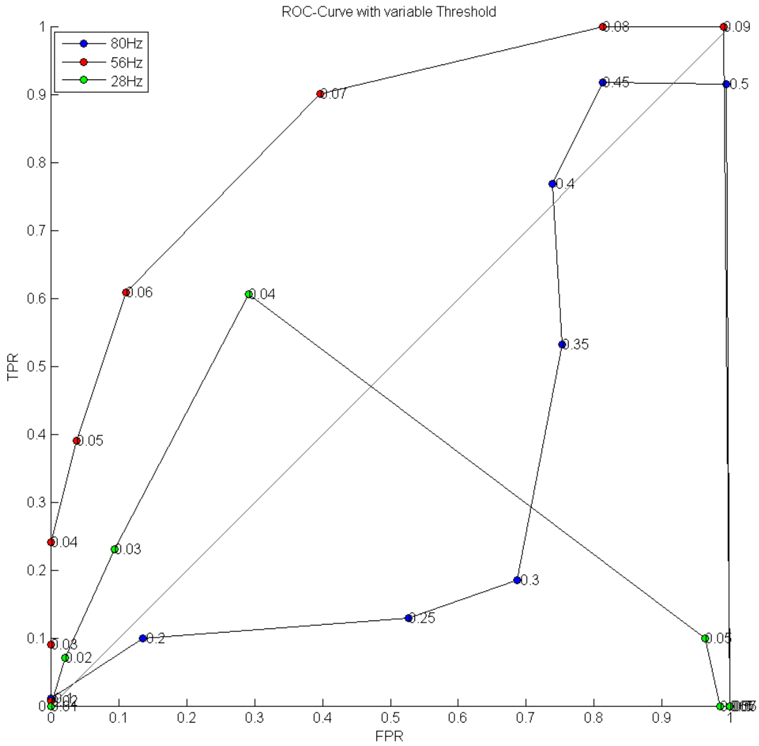

FIGURE A.2: ROC-curve of the true threshold values, without any method of automatically calculating the value.

the curve will not end in any of the expected corners. Therefore the ROC-curve Figure A.2 is created. This shows the true threshold values and all the boundary conditions are removed. This way there is too much detection when the threshold is too high but the algorithm will not neglect these detections this time. So the ROC-curve will detect these as false positives and shoot to the lower right corner.

Filters Wiener and Gauss filters are tested by creating ROC-curves in Figure A.3. The values in the graph represent the filters standard deviation. The filter size then becomes $S_s = 6\sigma$.

Region of interest The size of the ROI is varied in the x-direction as shown in Figure 2.15.

Boundary Conditions The three boundary conditions discussed in Chapter 2.3.1.3 are shown next in Figure A.5. Varied are the distance between pixels in the x and y direction inside the ROI.

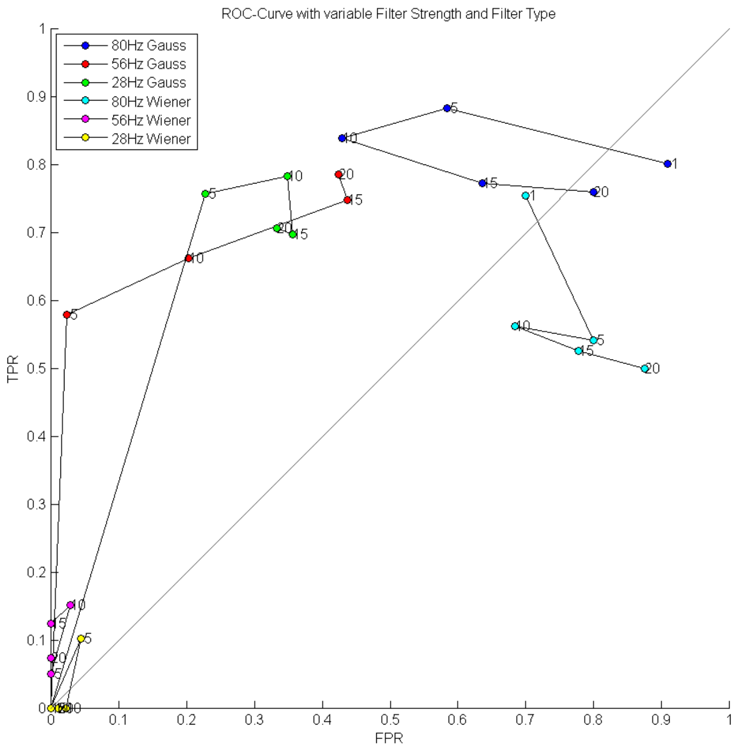

FIGURE A.3: ROC-Curve of the Wiener and Gauss filter with different standard deviations.

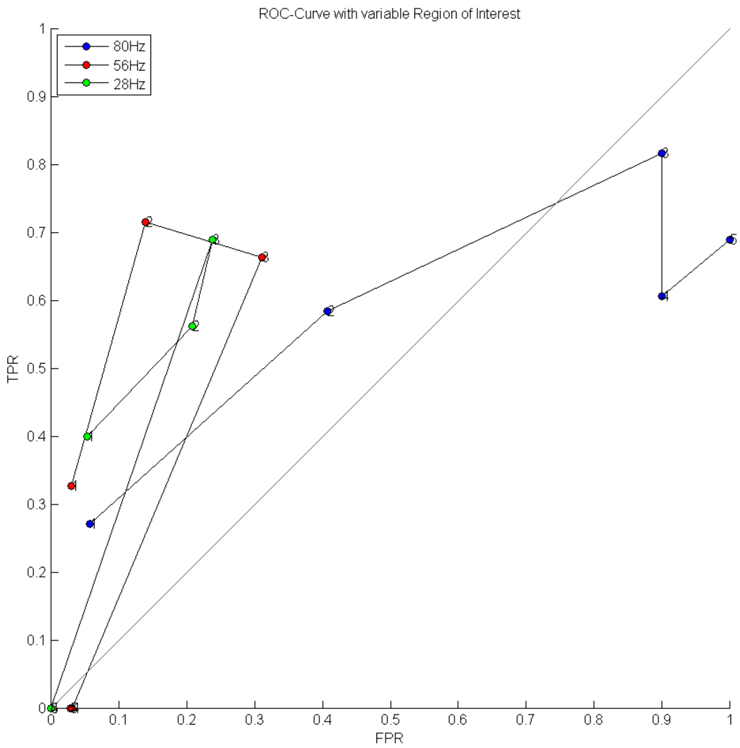

FIGURE A.4: ROC-curve of the region of interests size, increasing size in the X-direction in Figure 2.7.

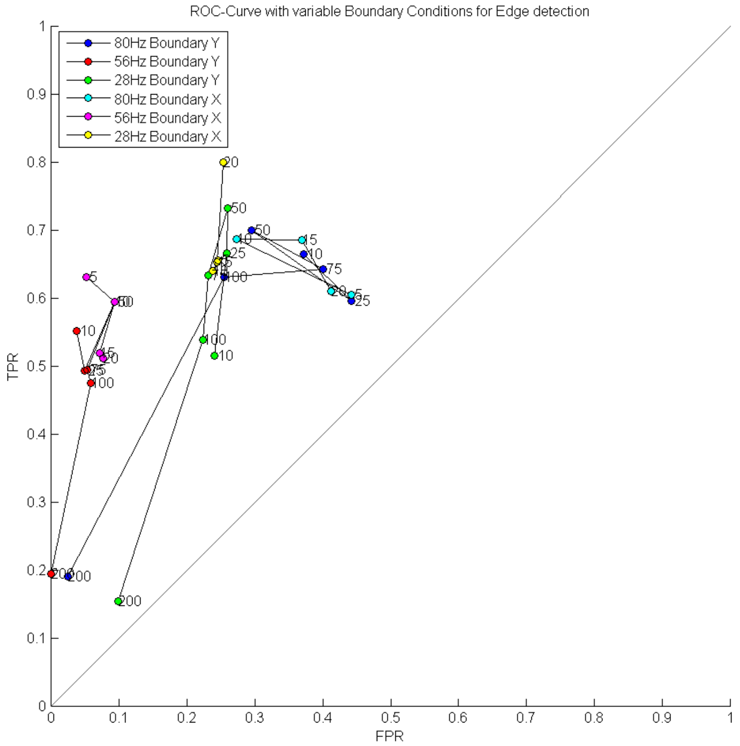

FIGURE A.5: ROC-curve of the size of the boundary conditions used for the edge detection. Boundary conditions for top, bottom and left side of the region of interest are included.

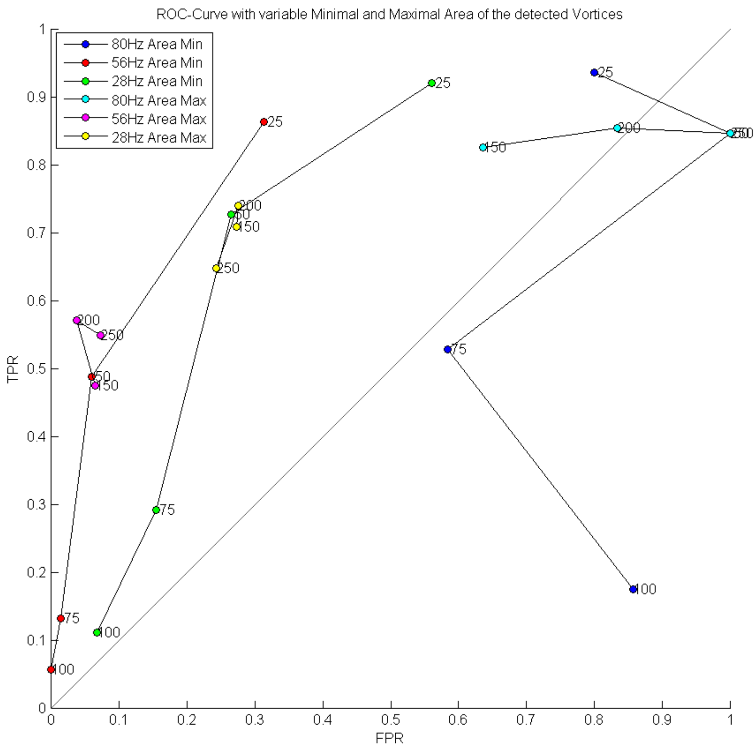

FIGURE A.6: ROC-curve of the minimal and maximal area size of the detections. When calculating the maximal area size, the minimal was kept constant and the same goes for the reverse.

Areas In Figure A.6 the ROC-curve is shown for the minimal and maximal area. The variable in the graph is squared to give the area.

Bibliography

[1] Aben, P. (2010). *High-amplitude thermo acoustic flow interacting with solid boundaries*. Phd thesis, TU Eindhoven.

[2] Backhaus, S. and Swift, G. (2000). A thermoacoustic-Stirling heat engine: detailed study. *The Journal of the Acoustical Society of America*, 107(6):3148–66.

[3] Bisio, G. and Rubatto, G. (1999). Sondhauss and Rijke oscillations—thermodynamic analysis, possible applications and analogies. *Energy*, 24(2):117–131.

[4] Boluriaan, S. and Morris, P. J. (2003). Acoustic streaming : from Rayleigh to today. *book*, 2(3):255–292.

[5] Ceperley, P. H. (1979). A pistonless Stirling engine - The traveling wave heat engine. *The Journal of the Acoustical Society of America*, 66(5):1508–1513.

[6] Ceperley, P. H. (1985). Gain and efficiency of a short traveling wave heat engine. *The Journal of the Acoustical Society of America*, 77(3).

[7] Dixhoorn, F. V. (2014). *Visualization and Pressure Measurements of the Oscillatory flow in a Jet Pump 1 Abstract*. Bachelor thesis, University of Twente.

[8] Feldman, K. (1968a). Review of the literature on Rijke thermoacoustic phenomena. *Journal of Sound and Vibration*, 7(1):83–89.

[9] Feldman, K. (1968b). Review of the literature on Sondhauss thermoacoustic phenomena. *Journal of Sound and Vibration*, 7(1):71–82.

[10] Gonzalez, R. C. and Woods, R. E. (2001). *Digital Image Processing*. Addison-Wesley Longman Publishing Co., Inc., Boston, MA, USA, 2nd edition.

[11] Gornowicz, G. (1997). *Continuous-field image-correlation velocimetry and its application to unsteady flow over an airfoil*. PhD thesis, California Institute of Technology.

[12] Gun, D. V. D. (2013). *Design and Realization of an Experimental Thermoacoustic Setup*. Master thesis, University of Twente.

[13] Hanley, J. A. and McNeil, B. . (1982). The Meaning and Use of the Area under a Receiver Operating (ROC) Curvel Characteristic. *Radiology*, 143(1):29–36.

[14] Hoare, F. E., Jackson, L., and Kurti, N. (1961). *Experimental cryophysics*. Butterworths, London.

[15] Huttenlocher, D., Noh, J., and Rucklidge, W. (1993). Tracking non-rigid objects in complex scenes. *1993 (4th) International Conference on Computer Vision*, pages 93–101.

[16] Iguchi, M., Ohmi, M., and Maegawa, K. (1982). Analysis of Free Oscillating Flow in a U-Shaped Tube. *Bulletin of JSME*, 25(207):1398–1405.

[17] Johnson, H. J. and Christensen, G. E. (2002). Consistent landmark and intensity-based image registration. *IEEE transactions on medical imaging*, 21(5):450–61.

[18] Kantorovich, L. V. (2006). On the Translocation of Masses. *Journal of Mathematical Sciences*, 133(4):1381–1382.

[19] Kapur, J., Sahoo, P., and Wong, A. (1985). A new method for gray-level picture thresholding using the entropy of the histogram. *Computer Vision, Graphics, and Image Processing*, 29(3):273–285.

[20] Kittler, J. and Illingworth, J. (1986). Minimum error thresholding. *Pattern recognition*, 19(1):41–47.

[21] Lamboo, S. (2013). *Setup Design for Flow Visualization of Oscillating Flow*. Bachelor thesis, University of Twente.

[22] Merzkirch, W. (1974). *Flow visualization / Wolfgang Merzkirch*. Academic Press, New York.

[23] Monge, G. (1781). *Mémoire sur la théorie des déblais et des remblais, avec les Mémoires de Mathématique et de Physique pour la même année*. De l'Imprimerie Royale, Paris.

[24] Nixon, M. (2008). *Feature extraction & image processing*. Newnes.

[25] Oberti, F. and Regazzoni, C. (2000). Adaptive tracking of multiple non-rigid objects in cluttered scenes. *Proceedings 15th International Conference on Pattern Recognition. ICPR-2000*, 3:1096–1099.

[26] Petculescu, A. and Wilen, L. a. (2003). Oscillatory flow in jet pumps: Nonlinear effects and minor losses. *The Journal of the Acoustical Society of America*, 113(3):1282.

[27] Radebaugh, R. (2000). Development of the Pulse Tube Refrigerator as an Efficient and Reliable Cryocooler. *Institute of Refrigeration*, page 1999.

[28] Rayleigh, J. (1896). *The Theory of Sound*. Number v. 2 in The Theory of Sound. Macmillan.

[29] Sezgin, M. and Sankur, B. (2004). Survey over image thresholding techniques and quantitative performance evaluation. *Journal of Electronic Imaging*, 13(1):146–165.

[30] Swift, G. (2004). What is thermoacoustics? A brief description, with technical details and citations. Technical report, Los Alamos National Laboratory.

[31] Swift, G. and Garret, S. (2003). Thermoacoustics: A Unifying Perspective for Some Engines and Refrigerators. *The Journal of the Acoustical Society in America*, 113(5):2379.

[32] Swift, G. W., Gardner, D. L., and Backhaus, S. (1999). Acoustic recovery of lost power in pulse tube refrigerators. *The Journal of the Acoustical Society in America*, 105(May 1998):711–724.

[33] Tian, Y. and Hampapur, A. (2005). Robust salient motion detection with complex background for real-time video surveillance. *... Vision, 2005. WACV/MOTIONS'05 ...*.

[34] Vidya, M. C. (2014). *Oscillatory Flow in Jet Pumps: Setup Design and Experiment*. Master thesis, University of Twente.

[35] West, C. D. (1983). *Liquid piston Stirling engines*. Industrial Engineering. Van Nostrand Reinhold.

[36] Westerweel, J., Fukushima, C., Pedersen, J. M., and Hunt, J. C. R. (2009). Momentum and scalar transport at the turbulent/non-turbulent interface of a jet. *Journal of Fluid Mechanics*, 631:199.

[37] Wiener, N. (1964). *Extrapolation, Interpolation, and Smoothing of Stationary Time Series*. The MIT Press.

[38] Wikipedia (2013). ROC-Curve.

[39] Wikipedia (2014). Schlieren Photography.

[40] Wixson, L. and Hansen, M. (2000). Detecting salient motion by accumulating directionally-consistent flow. *IEEE Transactions on Pattern Analysis and Machine Intelligence*, 22(8):774–780.

[41] Xing, C. and Qiu, P. (2011). Intensity-based image registration by nonparametric local smoothing. *... and Machine Intelligence, IEEE Transactions on*, pages 1–12.

[42] Yazaki, T., Iwata, A., Maekawa, T., and Tominaga, A. (1998). Traveling Wave Thermoacoustic Engine in a Looped Tube. *Phys. Rev. Lett.*, 81(15):3128–3131.

[43] Yazaki, T., Tominaga, A., and Narahara, Y. (1980). Experiments on thermally driven acoustic oscillations of gaseous helium. *Journal of Low Temperature Physics*, 41(1-2):45–60.

[44] Zack, G. W. and Rogers, E. (1977). Automatic Measurement of Sister Chromatid Exchange Frequency. *The Journal of the Histochemistry and Cytochemistry*, 25(7):11–14.

[45] Zhou, H., Yuan, Y., Zhang, Y., and Shi, C. (2009). Non-rigid object tracking in complex scenes. *Pattern Recognition Letters*, 30(2):98–102.

[46] Zhu, L., Haker, S., and Tannenbaum, A. (2013). Mass Preserving Registration for Heart MR Images. *Medical Image Computing and Computer-Assisted Intervention*, 8(0 2):147–154.

[47] Zhu, L., Yang, Y., Haker, S., and Tannenbaum, A. (2007). An image morphing technique based on optimal mass preserving mapping. *IEEE transactions on image processing : a publication of the IEEE Signal Processing Society*, 16(6):1481–95.